Eindhoven University of Technology

MASTER

The influence of rotation on the flow through a rectangular cavity

van Eekelen, E.C.M.

Award date:
2019

The influence of rotation on the flow through a rectangular cavity

Master thesis

ESTER VAN EEKELEN

Supervised by:
Dr. M Duran-Matute
Co-supervised by:
Prof. dr. L.R.M. Maas

Committe members:
Prof. dr. ir. G.J.F. van Heijst
Dr. J.H.E. Proll

March 5, 2019

Abstract

In this project, we have studied the influence of background rotation on the flow through a rectangular cavity via experiments and numerical simulations. The goal of this study is to determine if background rotation accelerates or retards the flow. It is found that the throughflow is retarded for increasing rotation rates. Visualizations and simulations show the emergence of large circulation cells and vortices. A cross-channel pressure difference is measured near the inlet of the container, investigating the presence of geostrophy and waves. The results are ambiguous due to the presence of vortices near the measurement location. Geostrophy is only found for the lowest flow rates and highest rotation rates. The effect of tilting the tank is also studied. Here, the throughflow is studied for a single flow rate. Results show an initial increase in the flow rate for low rotation rates and a decrease for higher rotation rates. However, in general, we observe that the throughflow is decreased for increasing rotation rates and that inertial waves are present. It is concluded that the effects of rotation on the throughflow are more delicate than previously thought. In fact, due to the limiting accuracy of the pump, we are unable to accurately quantify the effect of rotation on the mean throughflow.

Preface

This Master thesis is the written result of my graduation project at Eindhoven University of Technology. During my Master Applied Physics, my interest for the courses given by the Turbulence and Vortex Dynamics grew. It was clear to me that I wanted to do my graduation project within this group on an experimental study combined with simulations. The project I chose was challenging because besides performing experiments, a new setup would have to be built. During the project almost all parts of the setup broke down or appeared to work suboptimal which required a lot of patience and perseverance. Unfortunately, the complexity of the problem and setup lead to the fact that the setup is still not performing optimal. However, I am proud to say that I finished my graduation project and was able to determine what improvements on the setup are necessary to accurately study the problem in the future.

I would like to take this opportunity to express my gratitude to the people who helped me during the past year. First of all, I would like to thank my graduation supervisor Matias Duran-Matute, who assisted and guided me in this project during all setbacks. I would like to thank Leo Maas for starting the project and discussing the progress and results during the project. Also, I would like to thank the technical staff without whom I would never have been able to build my setup, Ad, Freek and Gerald, thank you for all your help and never ending knowledge. Special thanks goes to René, who supported me during my entire study and who is always there to cheer me up. Last but not least, I would like to thank my family, friends and fellow students for all the support throughout the year.

I hope you will enjoy reading this thesis.

Ester van Eekelen

Contents

Chapter 1

Introduction

An example of the impact of the earth's rotation can be seen in the northwestern Pacific (Figure 1.1), where a strong low pressure area is located. Due to the Coriolis force, the low pressure cell rotates counterclockwise on the Northern hemisphere and clockwise on the Southern hemisphere [1]. Besides the effects on these airflows, the rotation of earth also affects oceanic flows by the formation of waves [2]. Waves in a fluid can accelerate or retard the flow, influencing the energy efficiency of the fluid transport [3, 4]. In machinery, rotation can be used to save energy, and in fuel tanks in rockets, rotation inhibits the throughflow. This might cause engines to work suboptimal [5].
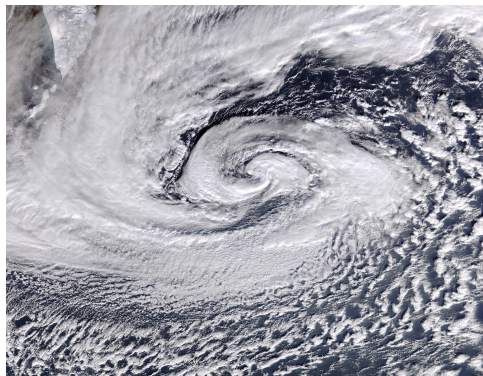
Figure 1.1: A strong low pressure system above the Northwestern Pacific on December 12, 2012. The rotation is in the counterclockwise direction. This photograph is obtained from [6].

When rotation is added to a flow, the flow is influenced and bent due to the Coriolis force. In a closed cavity, such as the fuel tank in a rocket, this rotation results in a circulation [7]. At the horizontal boundaries, an Ekman boundary layer arises as an effect of the rotation, resulting in a secondary circulation in the flow. Both these effects of rotation, the circulation due to the Coriolis force and the Ekman layers, need energy to be sustained [8, 9]. When energy is transferred to the secondary flow due to the Coriolis force and the Ekman layers, the throughflow is expected to decrease since this energy transfer is perceived as friction on the flow [7]. When instabilities arise in a rotating flow, they can lead to inertial waves to which energy is transferred [10]. Inertial waves have the property that their energy can be focused or defocused on a specific trajectory [11]. When the waves are focused, the energy is concentrated along this specific trajectory. This focusing of wave energy creates mixing of angular momentum that leads to a mean flow [12].

Under the right circumstances it is argued that this mean flow might as well support the throughflow in a closed system [3].

To understand how rotation affects the flow through a cavity, laboratory experiments and numerical simulations were previously performed [3, 13]. In these experiments, the flow through a rectangular container for various flow and rotation rates was investigated. In addition, the effect of a tilted cavity on the throughflow was investigated, and the cross-channel pressure differences were measured. In rotating fluids the ratio between the inertial forces and Coriolis force is described by the Rossby number $Ro = U/(fL)$ where U is the flow velocity, f the Coriolis parameter and L the characteristic length scale of the system. When $Ro > 1$ inertial forces dominate [3]. When $Ro < 1$, the Coriolis force dominates, inertial waves can be present, and the flow is assumed to be geostrophic. The throughflow for the experiments in a container without a tilt is observed to be decreased in the regime where $Ro > 1$ and enhanced in the inertial wave regime where $Ro < 1$ [3]. This is not in agreement with the simulations [13]. The simulations show a decrease in the throughflow for increasing rotation rates in the entire investigated parameter space. When the container is placed under an angle, observations showed that the throughflow is further enhanced for a larger parameter space. Using the cross-channel pressure difference, waves present in the flow can be identified by their frequencies. In the results, the rotation frequency of the rotating table is dominantly present, indicating a misalignment of the rotating table. This misalignment was later confirmed by using an accelerometer [14]. The misalignment raises questions about the accuracy of the measured throughflow. Since the flow will be further enhanced when a tilt is added, it is discussed whether the misalignment of the table causes an apparent tilt when the container is aligned horizontally [3].

The results from the previous experiments are ambiguous due to the misalignment of the table. Therefore, it is still not understood how the rotation affects the flow and if the fluid is transported in an energy efficient way. This study provides experiments and simulations on the same system with a stable setup to study how rotation affects the flow in a rectangular container. We study the throughflow in the container with and without background rotation for varying imposed flow rates and rotation rates. The experiments are compared to simulations for a single imposed nonrotating flow rate. To get insight in the flow field, visualizations are performed to obtain the flow structure. These flow structures are compared to streamlines from the simulations. To investigate what waves are present in the container, pressure measurements are performed. The measured differential pressure signal is studied by means of a frequency analysis to show the frequencies of the waves present in the container. From the results from [3] it is discussed whether a tilt increases the throughflow. To investigate this, the throughflow is measured for a tilted container and pressure measurements are done in search for waves.

In this report, we present results from experiments and simulations on the effect of rotation on the flow. In Chapter 2 the theoretical aspects of rotating fluids that are relevant for our study are discussed. In Chapter 3 we describe the experimental setup. In Chapter 4 the numerical setup is described, how the model is implemented and what variables are of importance to obtain trustworthy results from simulations. In Chapter 5 the results from the experiments and simulations are interpreted and discussed. In Chapter 6 we give the conclusion followed by the outlook in Chapter 7.

Chapter 2

Theory

This chapter presents a review of the theoretical aspects of rotating fluids that are relevant for our study. The starting point is the Navier-Stokes equation for the flow in a rotating reference frame. This equation includes the Coriolis and centrifugal forces and can be written as

$$\rho\frac{\partial \vec{u}}{\partial t} + \rho(\vec{u} \cdot \vec{\nabla})\vec{u} + 2\rho\vec{\Omega} \times \vec{u} = -\vec{\nabla}P + \rho\nu\nabla^2\vec{u} - \rho\vec{\nabla}(\frac{1}{2}\Omega^2 r^2), \qquad (2.1)$$

where ρ is the density, $\vec{u}$ is the velocity of the fluid, $\vec{\Omega} = (0,0,\Omega)$ the rotation rate of the system, P the pressure, ν the kinematic viscosity and r the radius from the rotation axis. The Coriolis force in eq. (2.1) is given by $2\rho\vec{\Omega} \times \vec{u}$, where the factor $f = 2\Omega$ is also known as the Coriolis parameter. The centrifugal force in eq. (2.1) is given by $-\rho\vec{\nabla}(\frac{1}{2}\Omega^2 r^2)$.

2.1   Geostrophic flow

We consider a rotating fluid with a constant density ρ in steady state where viscous effects are small enough to be neglected. A small amount of fluid, a fluid parcel, is moving forward in the x-direction with a velocity $\vec{v}$ as shown in Figure 2.1. Due to counterclockwise rotation, the Coriolis force F_{cor} acts on this moving fluid parcel and pulls the fluid parcel towards its right. Because this fluid parcel is pulled towards its right hand side, the pressure decreases at the left of the parcel and increases on the right of the parcel, creating a pressure gradient $\vec{\nabla}P$. This pressure gradient also acts on the fluid parcel by pulling it back towards its left.

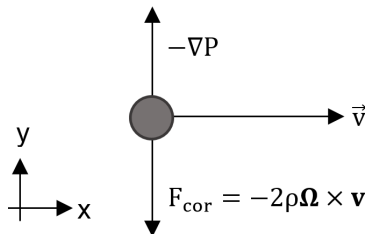Figure 2.1: The fluid parcel moves with a velocity $\vec{v}$ in the x-direction. Due to the Coriolis force F_{cor}, it is pulled towards its right, creating a pressure gradient $\vec{\nabla}P$. The pressure gradient pulls the fluid parcel towards its left. When these two forces are in equilibrium, the flow is in geostrophic balance, i.e. it is a geostrophic flow. This image is based on [1].

When these two forces, the pressure gradient and the Coriolis force, are in equilibrium the flow is called a geostrophic flow. The corresponding geostrophic balance can be obtained from the Navier-Stokes equation eq. 2.1 by assuming a steady state, neglecting viscous effects and neglecting local and convective acceleration terms [15]. The geostrophic balance is given by

$$fu = -\frac{1}{\rho}\frac{\partial P}{\partial y}, \tag{2.2}$$

$$-fv = -\frac{1}{\rho}\frac{\partial P}{\partial x}, \tag{2.3}$$

$$0 = -\frac{1}{\rho}\frac{\partial P}{\partial z}, \tag{2.4}$$

where u and v are the velocity components in the x and y direction, respectively. The flow is assumed incompressible so $\vec{\nabla} \cdot \vec{v} = 0$. From the geostrophic balance, it is derived that

$$\frac{\partial u}{\partial z} = \frac{\partial v}{\partial z} = \frac{\partial w}{\partial z} = 0. \tag{2.5}$$

This is also known as the Taylor-Proudman theorem, which shows that in a geostrophic balance the flow is uniform perpendicular to the rotation axis [16].

2.2 Inertial waves

Inertial waves arise in an incompressible, homogeneous, rotating fluid. For each radius from the rotation axis, the fluid at that radius has a specific angular momentum: the angular momentum is stratified in the radial direction. The restoring force in the inertial waves is the Coriolis force [17]. To describe inertial waves, we will first consider forces acting on a particle having the same density as the fluid. Inertial waves occur when a fluid parcel in a rotating flow is slightly perturbed outward from its radial position. Due to the conservation of angular momentum, the angular momentum of the fluid parcel will be lower than the angular momentum at its new position. Therefore, the parcels velocity will be lower and the centrifugal force is no longer in equilibrium with the inward pressure. Hence, the parcel will be restored due to the Coriolis force and start to move in a circular motion in the xy-plane, perpendicular to the rotation axis. If we now start considering the medium is a continuum where the continuity equation $\vec{\nabla} \cdot \vec{v} = 0$ is valid, we know that this motion in the xy-plane disturbs particles in the z-direction creating a pressure gradient in the z-direction. As an effect of this, the particle will move in a circular motion in a tilted plane. Due to this motion, surrounding particles are perturbed as well and will start to move in the same plane but at a shifted phase. The wave resulting from a localized disturbance is an inertial wave which has a conical shape. A cross section of the conical inertial wave is shown in Figure 2.2, where the velocity field is shown by the arrows and the axial vorticity is given by the colors [18].
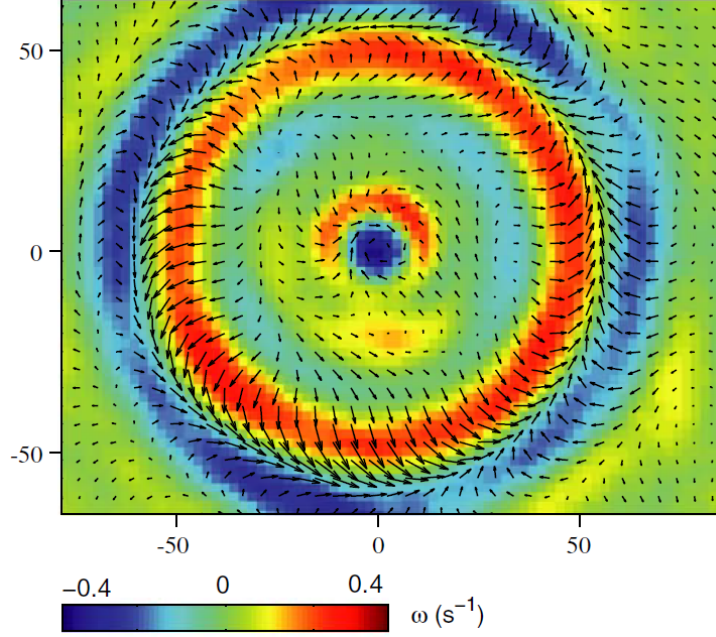
Figure 2.2: The cross section of an inertial wave at a certain height below the location where a periodic perturbation is performed. The velocity field is given by arrows and the axial vorticity field ω_z is given with the colors. The forcing frequency is equal to $\omega/2\Omega = 0.74$. This image is obtained from [18].

The momentum equations of the inertial waves are given by

$$\frac{\partial u}{\partial t} - fv = -\frac{1}{\rho}\frac{\partial P}{\partial x}, \tag{2.6}$$

$$\frac{\partial v}{\partial t} + fu = -\frac{1}{\rho}\frac{\partial P}{\partial y}, \tag{2.7}$$

$$\frac{\partial w}{\partial t} = -\frac{1}{\rho}\frac{\partial P}{\partial z}. \tag{2.8}$$

The dispersion relation can be determined from these equations and is given by [19]

$$\omega = \pm 2\Omega \sin(\theta). \tag{2.9}$$

Here ω is the wave frequency and θ is the constant angle under which the wave energy propagates with respect to the rotation axis. Inertial waves are low frequency waves which means that they propagate with a frequency lower than the Coriolis frequency $f = 2\Omega$ as can be seen by the dispersion relation. Note that the angle θ under which the waves propagate is only dependent on the rotation frequency Ω and the frequency of the waves ω. The phase velocity of the inertial waves $\vec{c}$ is given by

$$\vec{c} = \frac{2(\vec{k} \cdot \vec{\Omega})}{\mid \vec{k} \mid^3}, \tag{2.10}$$

where $\vec{k}$ is the wave vector. The group velocity $\vec{c_g}$ is perpendicular to the phase velocity $\vec{c}$ and is given by

$$\vec{c_g} = \pm\frac{2\vec{k} \times (\vec{\Omega} \times \vec{k})}{\mid \vec{k} \mid^3}. \tag{2.11}$$

The energy of the inertial waves travels along the group velocity.

2.2.1 Wave attractor

From eq. 2.9 we know that the angle θ under which the inertial waves propagate only depends on the wave frequency ω and the rotation frequency Ω. When the inertial waves hit a boundary, they reflect with this constant angle that is not dependent on the angle of the boundary as schematically shown in Figure 2.3. The reflection at a horizontal boundary is shown in Figure 2.3(a), and at sloping boundary in Figure 2.3(b). As seen from the figure for a sloping boundary, the waves and energy can converge or diverge. In Figure 2.3(b), when the waves are moving from left to right, they are focusing, and when they are moving from right to left they are defocussing. In convex fluid domains, focusing dominates over defocussing of the waves [11].
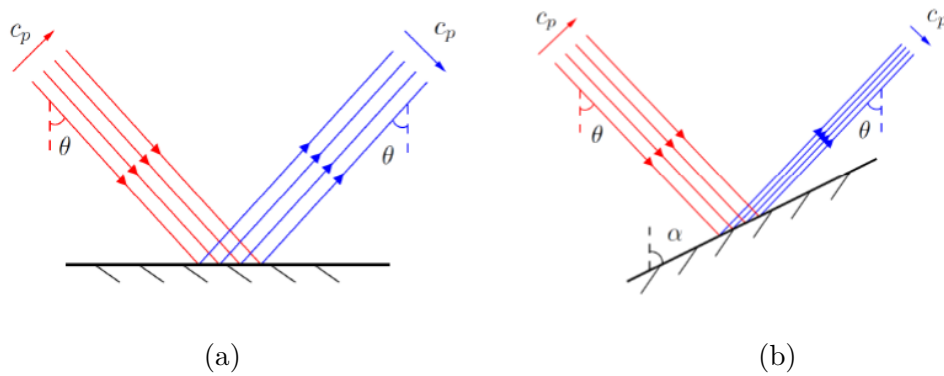

(a)   (b)

Figure 2.3: Reflection of waves and energy by hitting a boundary. The boundary in (a) is horizontal and in (b) under angle α. The waves have a constant propagation angle θ and the phase propagation is given with c_p. In (b), the waves focus when they move from left to right and defocus when they move from right to left [20]

The energy in inertial waves moves in the direction of the group velocity $\vec{c_g}$, i.e. along the rays depicted in Figure 2.3. In a closed system, after a certain amount of reflections, all waves and thus the energy follow the same path. This limit cycle is called a wave attractor. An example of this is shown in Figure 2.4. Here a trapezoidal domain is considered, with two starting positions of the waves noted with the red and blue rectangles [20]. The waves converge when they hit the sloping boundary on the left. After a certain amount of reflections both rays converge to the same limit cycle: the wave attractor noted with the black line in Figure 2.4. These wave attractors have been found previously in a trapezoidal domain [21] and in a tilted container with a square cross section [22, 23]. In experiments, it is found that after an amount of reflections, mixing of angular momentum occurs. This leads to centrifugal instabilities creating an additional cyclonic mean flow in the domain [12].
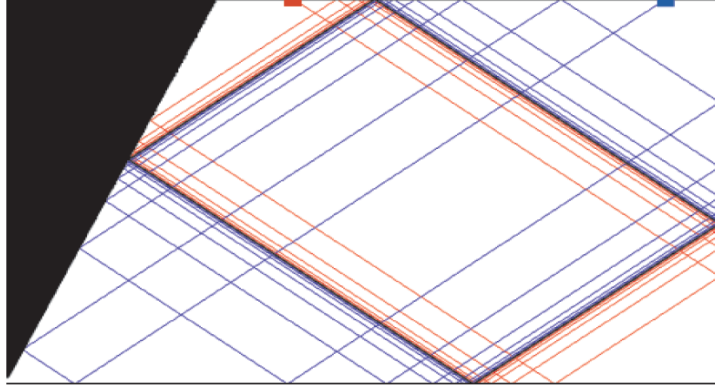
Figure 2.4: Example of a wave attractor in a trapezoidal domain. Two waves are traced starting at two different start positions, noted with the red and blue rectangles. The waves converge when they hit the sloping boundary independently of their starting position. Both rays end in a limit cycle: the wave attractor, noted with the black line. This image is obtained from [20].

2.3   Rossby waves

Rossby waves are low frequency waves and can theoretically be derived from the conservation of potential vorticity. As stated by Ertel's theorem [24], this can be expressed as

$$\frac{D\Pi}{Dt} = \frac{D}{Dt}\left(\frac{\zeta + f}{H}\right) = 0, \tag{2.12}$$

where D/Dt is the material derivative, Π is the potential vorticity, ζ is the relative vorticity, f is the Coriolis parameter, and H is the depth of the water column.

Due to the conservation of potential vorticity, a change in the relative vorticity ζ can only be caused by a change in the height H or in the Coriolis parameter f. Since the rotation rate is constant and uniform in a laboratory, the Coriolis parameter is constant. This means that a change in relative vorticity can only be caused by a change in the water depth H. This happens when the container is tilted as shown in Figure 2.5. In oceanic flows, H is constant and f is the variable parameter that changes with the latitude ϕ as $f = 2\Omega\sin(\phi)$. Hence, moving to the North increases f and to the South decreases f. Therefore, by mapping the topographic Rossby waves to planetary Rossby waves, we can associate the shallow part of the container with the North and the deep part with the South.
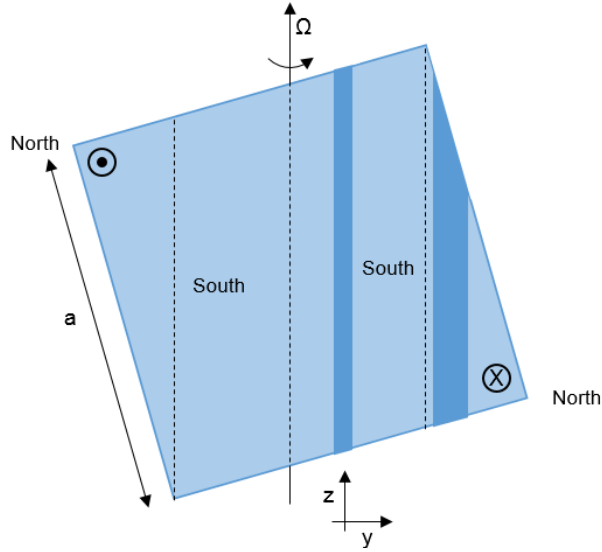
Figure 2.5: Schematic view of the tilted tank. The shallow part of the container corresponds to the North, the deep part to the South. The tank is rotated with frequency Ω. The vortex tubes are compressed moving upwards the sloping bottom generating a decrease in the relative vorticity. This generates topographic Rossby waves that propagate in the westward direction noted by the directions in the corners of the tank [15].

To understand how the Rossby waves occur, a perturbed string of fluid parcels is considered as shown in Figure 2.6. These fluid parcels correspond to vertical vortex columns as shown in Figure 2.5. For parcels that are perturbed towards the shallow part of the container (the North), the depth H decreases and the vortex column is squeezed. Hence, to conserve potential vorticity, $D\zeta/Dt < 0$ and the fluid parcels acquire negative vorticity, noted in Figure 2.6 with a minus sign. For the perturbed fluid parcels in the deep part of the container (the South), the depth H increases, the vortex column is stretched, and therefore, $D\zeta/Dt > 0$. Hence, the fluid parcels acquire positive vorticity noted in Figure 2.6 with the plus sign. Due to the gained negative and positive vorticity, the perturbed string will act as vortices, resulting in a westward propagation of the wave and stretching and squeezing of the vortex tubes [15, 25]. These waves are know as topographic Rossby waves and have the same propagation principle as planetary Rossby waves in which H is constant and f varies.
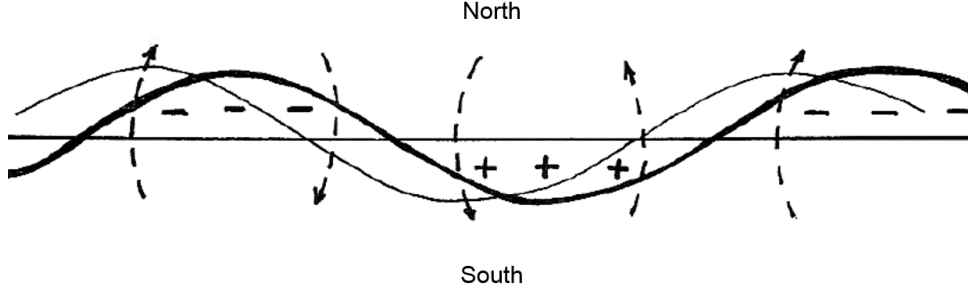
Figure 2.6: A string of fluid parcels is perturbed in a sinus shape. The parcels perturbed to the North gain negative relative vorticity noted with the minus sign and the ones to the South gain positive relative vorticity noted with the plus sign. Due to this gained vorticity the string will act as vortices by which the Rossby wave will propagate in the westward direction [25].

As mentioned before, Rossby waves are low-frequency waves. On the earth, for a small change in latitude, f is approximated by a Taylor series around a fixed Coriolis parameter f_0. This results in $f = f_0 + \beta y$ known as the β-plane approximation. In laboratories, f is constant but a bottom topography is present. The small changes in H will be approximated by making a similar β-plane approximation and writing $\beta(H)$. With the tilted container shown in Figure 2.5 under an angle α, the height in the corners changes with a slope $s = (\tan(\alpha) - 1/\tan(\alpha))$. The height of the fluid outside the corners is $H_0 = a/\cos(\alpha)$ with a the length of the sides. Combining this, β can be written as

$$\beta = \frac{2\Omega \cos(\alpha)(\tan(\alpha) - 1/\tan(\alpha))}{a} = \frac{2\Omega \cos(\alpha)s}{a}. \tag{2.13}$$

The dispersion relation for Rossby waves is given by

$$\omega = \vec{u}m - \frac{\beta m}{m^2 + n^2}, \tag{2.14}$$

where ω is the wave frequency, and m and n are the wave numbers [25]. The frequency domain in which Rossby waves are present can be calculated from this dispersion relation. First we assume $\vec{u} = 0$, an angle $\alpha = 20°$, a length $a = 0.1$ m and the maximum sizes of the container of 0.1 and 0.2 m which gives $m = 2\pi/0.1$ and $n = 2\pi/0.2$. Secondly, by dividing ω by the rotation frequency 2Ω we obtain a maximum reduced frequency independent of the rotation frequency

$$\frac{\omega}{2\Omega} = 0.37. \tag{2.15}$$

Hence Rossby waves can be present for $0 \leq \omega/2\Omega \leq 0.37$.

2.4 Ekman boundary layer

Near a boundary in a rotating fluid, viscous effects become of importance [1, 15]. On the solid boundary, we have a no-slip condition so the velocity is zero at the boundary. A geostrophic flow cannot satisfy this boundary condition. The momentum equations inside the boundary layer can be obtained from the Navier-Stokes equation. In the boundary layer, a steady sate is assumed and nonlinear accelerations are neglected. The thickness of

the boundary layer is small, and therefore, the horizontal scale in the xy-direction is larger than the vertical in the z-direction. Hence, $\nabla^2 = \partial^2/\partial x^2 + \partial^2/\partial y^2 + \partial^2/\partial z^2 \approx \partial^2/\partial z^2$. The dimensionless momentum equations in the boundary layer resulting from this are

$$2u = -\frac{\partial P}{\partial y} + E\frac{\partial^2 v}{\partial z^2}, \tag{2.16}$$

$$-2v = -\frac{\partial P}{\partial x} + E\frac{\partial^2 u}{\partial z^2}, \tag{2.17}$$

$$0 = -\frac{\partial P}{\partial z} + E\frac{\partial^2 w}{\partial z^2}. \tag{2.18}$$

Here $E = \nu/\Omega L^2$ is the Ekman number with L the characteristic length scale of the system [2, 15]. The typical non-dimensional thickness δ of the Ekman boundary layer is given by

$$\delta = \sqrt{E}, \tag{2.19}$$

while the physical thickness of the boundary layer δ_E is expressed by

$$\delta_E = \sqrt{\frac{\nu}{\Omega}}. \tag{2.20}$$

Note that δ_E is independent of the typical length scale L of the system and the velocity of the flow [15]. By matching the pressure of the Ekman boundary layer to that in the interior of the fluid it is found that

$$\frac{\partial p_B}{\partial z} = 0, \tag{2.21}$$

where p_B is the pressure in the boundary layer [1]. This leads to $p_B = p_B(x, y) = p_I(x, y)$ where p_I is the pressure inside the interior of the fluid. Hence, the pressure in the boundary layer and in the interior of the fluid are equal. The momentum equations in the boundary layer are matched to those the interior of the fluid at the boundary interface. At this boundary interface, the geostrophic balance given in eq. (2.2) and (2.3) is valid [1, 26]. Using these conditions, the momentum equations can be rewritten as

$$2u = 2u_I + E\frac{\partial^2 v}{\partial z^2}, \tag{2.22}$$

$$-2v = -2v_I + E\frac{\partial^2 u}{\partial z^2}. \tag{2.23}$$

Here the subscript I is used for properties of the interior of the fluid. From these equations, the velocities in the x and y-direction can be obtained. Using the continuity equation, it is found that the Ekman layer also produces a velocity in the z-direction [1]. Since $\partial w/\partial z = 0$ as given in eq. 2.5, the flow has be constant through the entire depth of the fluid [26]. Hence, the Ekman layer produces a secondary circulation of the flow between the top and bottom boundary.

2.4.1 Tilted boundary layer

The Ekman boundary layer that we have described in the previous section is for horizontal boundaries, perpendicular to the axis of rotation. When the container is tilted under an angle α, the boundaries are no longer oriented horizontally and neither is the

Ekman layer as shown in Figure 2.7. For a tilt of $\alpha = \pi/2$, the boundaries are perfectly vertically oriented. This boundary layer on the vertical boundaries is known as the Stewartson layer [27]. The Stewartson layer with non-dimensional thickness δ_S, scales with the Ekman number as $\delta_S = E^{1/3}$.

A tilted boundary layer between the horizontal Ekman layer and the vertical Stewartson layer under an angle α is shown in Figure 2.7. When the tilt satisfies $\pi/2 - \alpha = \mathcal{O}(1)$, the boundary layer can be described using the horizontal Ekman layer [28]. Therefore, the local coordinate system (x^*, y^*, z^*) is introduced. This gives a rotation vector $\vec{\Omega} = (-\sin(\alpha), 0, \cos(\alpha))\Omega$ in the local coordinate system. With this local coordinate system, the momentum equations can be rewritten following the same steps as described in section 2.4. It follows from the momentum equations of the local coordinate system that the thickness of the tilted Ekman layer $\delta^* = E^{1/2}\sec(\alpha)^{1/2}$ [28]. The thickness of the Ekman layer is close to the non-tilted Ekman thickness for a small angle α. For example, for a tilt of $\alpha = 30°$, this gives $\delta^* = E^{1/2}\sec(\pi/6)^{1/2} = E^{1/2} \cdot 1.07$.
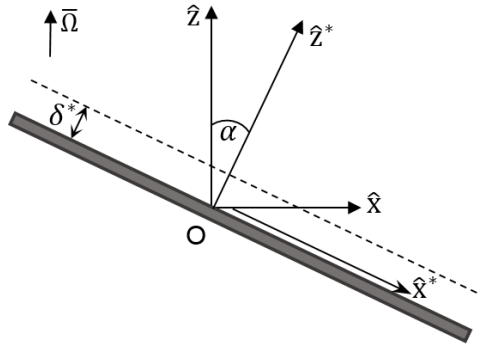

Figure 2.7: Tilted boundary under an angle α. A local coordinate system (x^*, y^*, z^*) is introduced. The thickness of the tiled Ekman boundary layer is $\delta^* = E^{1/2}\sec(\alpha)^{1/2}$. This image is based on [28].

Chapter 3

Experimental setup

In order to investigate the effect of rotation on the flow in a rectangular cavity, we build a setup which is shown schematically in Figure 3.1 from the side and top view.
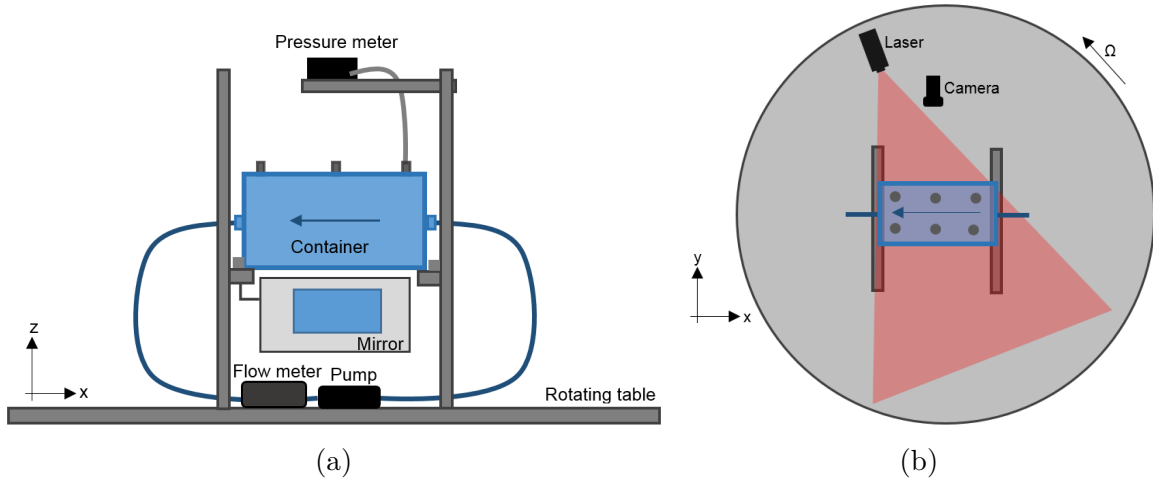

<div style="text-align:center">(a) (b)</div>

Figure 3.1: Schematic overview of the setup. In (a) the side view of the setup is shown, with the position of the container, mirror, pump, flow meter and pressure meter are visible on the rotating table. In (b) the top view of the setup in which the laser and camera directed to the container are visible. The blue arrow in the container in (a) and (b) gives the direction of the flow.

The setup is built on a stable rotating table that can rotate from 0 - 10 rad/s. The container, with dimensions of $20 \times 10 \times 10$ cm^3, is placed in the center of the table. At the top surface of the container, eight orifices are present as shown in the photo in Figure 3.2. The pump is used to create a flow in the container and the flow range can be controlled by applying a voltage between 5.4 and 10.2 V on the pump. The flow range that corresponds to this voltage range depends on both the inlet height of the container and the total length of the tubes that connect the in- and outlet of the container to the flow meter and the pump. With the inlet height and tube length of our setup, the flow range is 1.5 - 3.1 l/min. Lower flow rates can be reached by squeezing the tube with a clamp. Using this clamp, the entire flow range for the setup is 0.5 - 3.1 l/min. The flow rate is measured using a flow meter. The flow rate Q in l/min scales with output voltage of the flow meter V_O in volts as

$$Q = V_O \cdot 1.09 - 0.17. \tag{3.1}$$

The accuracy of the flow meter is ±0.05 l/min and the flow signal is recorded with a sampling rate of 100 Hz.
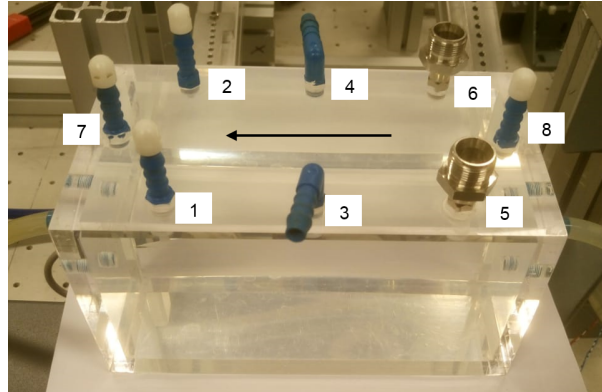

Figure 3.2: Photo of the container with the eight orifices on the lid numbered from 1 to 8. The arrow gives the direction of the flow.

A GE Druck LPM 5480 differential pressure meter is installed above the container and connected to orifices 5 and 6. This pressure meter measures the pressure difference between these two orifices as a function of time. The range of the differential pressure meter is approximately -25 to 25 Pa. The pressure P in Pa scales with the output voltage of the pressure meter V_P in Volts as

$$P = V_P \cdot 5.35 + 1.81. \tag{3.2}$$

The accuracy of the pressure meter is within 1 %, and the pressure signal is recorded with a sampling rate of 100 Hz. The pressure difference is used to determine whether the mean flow is in geostrophic balance as described in section 2.1 and to investigate what type of waves are present within the container. The pressure difference is averaged over time to order to determine the presence of geostrophy. A Fourier analysis on the pressure signal is performed to study the presence of waves. The frequencies of the waves present in the container are visible in the Fourier spectrum.

To visualize the flow inside the container a laser, mirror and camera are used. The laser shines a horizontal sheet on the container, lighting a horizontal plane as shown in Figure 3.1(b). The dirt particles in the container on this horizontal plane are made luminescent by scattering the light of the laser. Since the orifices are present on the top side of the container, the visualization is recorded from below. Using a mirror underneath the container allows us to record from below the container without placing the container at a significant height above the rotating table. The particles in the plane illuminated by the laser sheet are recorded by a camera directed at the mirror. Since we are only interested in the particles that move, it is necessary to remove all bright, stationary spots from the images by applying a background correction. This background is calculated by summing N frames and dividing this by N, i.e. by averaging the image over N frames. Then this background is subtracted from all frames that we have analyzed. Next, 100 frames are added to create a flow pattern. These 100 frames span approximately 3.0 s. The used Matlab scripts to obtain this flow pattern can be found in Appendix A.

3.1 Positioning of the individual components

Initially, the area below the container was aimed to be empty to place the camera underneath the container. Hence, the pump and flow meter were positioned alongside the container as shown in Figure 3.3. The pressure meter is placed on one of the pillars supporting the container. During the measurements, inconsistencies in the recorded flow rate became visible. These inconsistencies could be caused by effects of the rotation on the flow circuit, since it was not centered. This will be discussed in section 5.1. Hence, the circuit was relocated by using the space underneath the container instead of alongside as shown in Figure 3.1. The pressure meter is placed in the center of the table above the container, and the pump is placed in the center of the table underneath the container. The tubing goes directly downward from the container as straight as possible and the flow meter is positioned close to the pump. The new orientation of the circuit is aimed at keeping the tubings in the xz-plane to diminish the effects of rotation in the tubing.
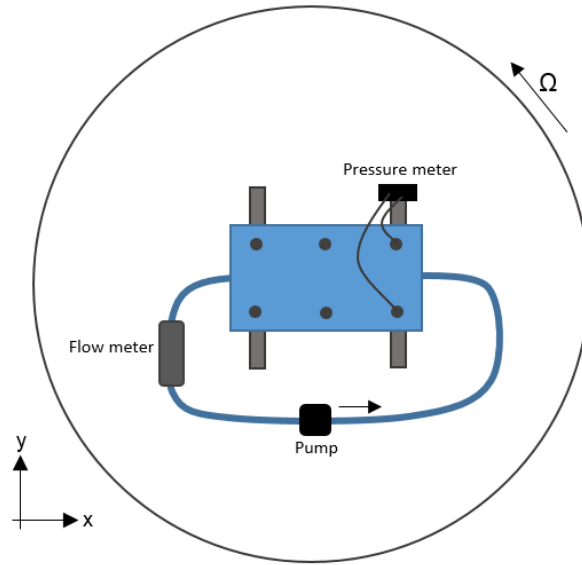

Figure 3.3: Schematic top view of the initial setup. The container is placed in the center of the rotating table, the pump, pressure meter and flow meter are placed off-center.

3.2 Connection of the pressure meter

The pressure meter is connected to the orifices 5 and 6 (shown in Figure 3.2) to measure the pressure difference between these two orifices as a function of time. The pressure meter is only able to measure pressure difference in a gas, not in water. Therefore, the pressure meter is connected with two long tubes to each of the orifices, which are filled with air on the pressure meter side. Since the opening of the orifices are small, the first few centimeters of the tube is filled with water directly connected to the water in the container. The inner diameter of the tubing that can be connected to the pressure meter is 4 mm. Capillary forces can inhibit the measurement of the pressure difference due to the smallness of the tubing diameter. Therefore, the tubing is connected to another tube with an inner diameter of 8 mm to remove the dominant effect of the capillary forces. A photo of the connecting tubings of the pressure meter to the container can be found in Figure 3.4. In this thicker tubing that is directly connected to the orifices, water is

present. A small floating cylinder is placed on top of the water surface in the thick tubings to counteract any effect due to surface waves. These small floating cylinders are visible in Figure 3.4 in the thick tubing as black disks.

It was noticed the pressure difference exceeded the maximum pressure difference that could be measured when the tubings were connected. This was caused by some small amount of air that is compressed by connecting the tubes to the pressure meter. The amount of air is not exactly equal for both tubes giving a rise in the pressure difference, resulting in a saturated pressure meter inhibiting any measurements. To get rid of this pressure difference when the tubes are connected, a valve is mount in each of the tubes as shown in Figure 3.4. These valves can be opened to let the compressed air out until the air inside the tube has the same pressure as the air in the room.
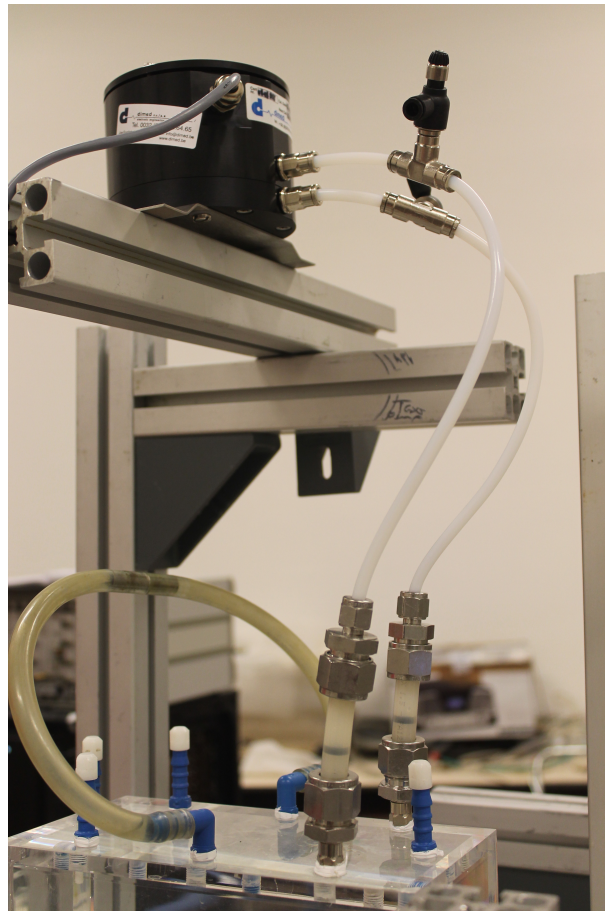
Figure 3.4: Photo of the connection of the pressure meter to the container. The thick tubes (diameter of 8 mm) are connected to the container and via a thinner tube (diameter of 4 mm) connected to the pressure meter. A valve is mound in the thin tube to get the pressure in the tube equal to the room. In the thick tubes two floating cylinders are present to counteract any surface waves.

3.3 Tilting the container

The container is mount on a base that allows tilting as shown in Figure 3.1. This tilted container is used to study if wave attractors or Rossby waves can play a role in the

flow through the container. By applying a voltage to the pump, it generates a flow. As mentioned before, the flow rate corresponding to a voltage on the pump is dependent on the tube length and the height of the container. To be able to compare the measurements on a tilted container to the ones without a tilt, the entrance height should be kept constant. In this way, the pump generates the same flow rate for the same applied voltage with and without tilt.

Chapter 4

Numerical setup

Simulations are performed using Comsol Multiphysics to get better insight in the flow inside the container and to check the results of the experiments. The Finite element solver tailored for solving the Navier-stokes equations is used to solve our model [29]. This finite element solver solves partial differential equations for a predefined grid. The simulations are performed using the time-dependent solver and use the laminar flow interface of Comsol. In this chapter we first describe the used model followed by the specifics of the simulations.

4.1 Description of the model

To simulate a flow, Comsol is used to solve the Navier-Stokes equation and the continuity equation:

$$\rho\frac{\partial \vec{u}}{\partial t} + \rho(\vec{u}\cdot\vec{\nabla})\vec{u} = \vec{\nabla}\cdot\left[-P\vec{I} + \mu(\vec{\nabla}\vec{u} + (\vec{\nabla}\vec{u})^T)\right] + \vec{F}, \tag{4.1}$$

$$\rho\vec{\nabla}\cdot\vec{u} = 0, \tag{4.2}$$

where ρ is the density of the fluid, $\vec{u}$ is the velocity of the flow, P is the pressure, $\vec{I}$ is the identity tensor, μ is the dynamic viscosity of the fluid, and $\vec{F}$ is the sum of all additional forces. In this case, the additional forces are the Coriolis force and the centrifugal force that are consequences of rotation in the flow. These two terms are, respectively, given by

$$F_{cor} = 2\vec{\Omega}\times\vec{v}, \tag{4.3}$$

$$F_{centr} = \vec{\nabla}(\frac{1}{2}\Omega^2 r^2). \tag{4.4}$$

The centrifugal force is left explicitly in the Navier-Stokes equation instead of in the pressure term. This because initially we wanted to vary the centrifugal force independently from the Coriolis force to see the effect when the rotation axis is out-of-center. Substituting the two terms to the Navier-Stokes equation and rewriting eq. (4.2) gives

$$\frac{\partial \vec{u}}{\partial t} + (\vec{u}\cdot\vec{\nabla})\vec{u} + 2\vec{\Omega}\times\vec{v} = -\frac{1}{\rho}\vec{\nabla}P + \nu\vec{\nabla}^2\vec{u} - \vec{\nabla}(\frac{1}{2}\Omega^2 r^2). \tag{4.5}$$

The simulations are performed in a dimensionless space. Therefore, dimensionless variables are implemented in the Navier-Stokes equation. These dimensionless variables denoted with primes, are given by

$$\vec{u} = \frac{\nu}{L}\vec{u}', \quad P = \Delta P P', \quad t = \frac{Lt'}{U}, \quad r = Lr', \quad \vec{\nabla} = \frac{\vec{\nabla}'}{L}, \tag{4.6}$$

where L is the characteristic length scale and nu the kinematic viscosity. Implementing these variables in the Navier-Stokes equation in eq. (4.5) gives

$$\frac{\partial \vec{u}'}{\partial t'} + (\vec{u}' \cdot \vec{\nabla}')\vec{u}' + E^{-1}2\vec{k} \times \vec{u}' = P_0\vec{\nabla}'P' + \nabla'^2\vec{u}' + E^{-2}\vec{\nabla}'r'^2, \qquad (4.7)$$

where $\vec{k} = \frac{\vec{\Omega}}{|\vec{\Omega}|}$ is the unit vector in the axial direction and $P_0 = -\Delta P L^2/2\rho\nu^2$. Comparing the dimensionless Navier-Stokes in eq. (4.7) to eq. (4.5), it can be seen that the characteristic pressure P_0 and the Ekman number, $E = \nu/(\Omega L^2)$ are the only two remaining parameters that are used to describe the flow. The pressure P_0 is used to create a flow by setting the initial pressure difference between the in- and outlet of the container. The Ekman number E is used to add rotation to the flow. The specific values of the pressure and the Ekman number and how they are determined is discussed later in this chapter.

4.1.1 Geometry of the container

In the model, the geometry of the container is implemented as shown in Figure 4.1. The length of the container in the simulations, in the x-direction equals 2, while the height in the z-direction and width in the y-direction are set to 1. These values are proportional to the real sizes which equal a length × width × height of $20 \times 10 \times 10$ cm³. The center of the container is placed at $(x, y, z) = (0, 0, 0)$ to get the same rotation axis in the simulations as in the experiments. The in- and outlet of the container are created by adding two cylinders to the container. In Figure 4.1 only the inlet is visible. The inlet is placed at $(x, y, z) = (-1, 0, 0)$ and the outlet at $(x, y, z) = (1, 0, 0)$. The diameter of the cylinders is equal to 0.05 which is equivalent to the diameter of the inlet in the experiments which equals 5 mm.
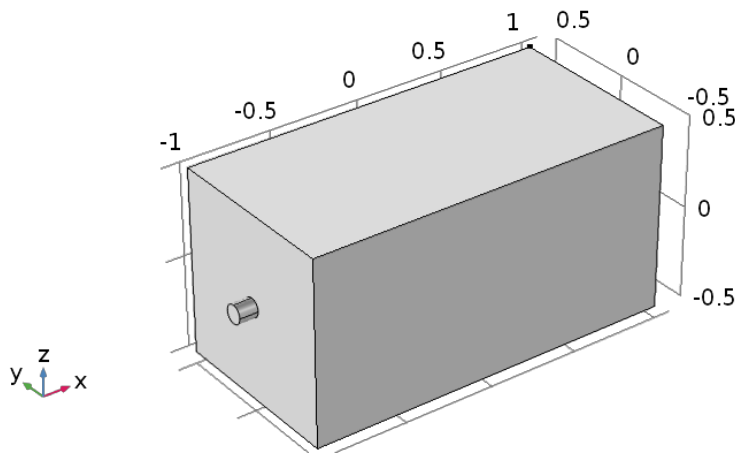

Figure 4.1: Geometry of the container in the simulations. The dimensions of the container are $2 \times 1 \times 1$. The in- and outlet are cylinders added to the container on respectively the coordinates $(x, y, z) = (-1, 0, 0)$ and $(x, y, z) = (1, 0, 0)$. The inlet is visible in this image. The center of the container is placed at the coordinates $(x, y, z) = (0, 0, 0)$ to get the same rotation axis in the simulations as in the experiments.

4.1.2 Boundary conditions

On the boundaries of the container, a no slip condition is imposed, i.e. the velocity at the boundary is set to zero. At the inlet and outlet, the boundary conditions are set

by the pressure. To generate a flow, a pressure difference is imposed between the inlet and the outlet. At the inlet, $P = P_0$ and at the outlet, $P = 0$. Additionally, the back flow is suppressed at the outlet. This prevents fluid to flow back from the outlet into the container. Using the back-flow suppression alters the pressure in the outlet locally.

4.2 Mesh configuration and resolution

The mesh used to compute the result consists of mesh elements that are tetrahedral in shape. An example of the mesh on the outside of the container is seen in Figure 4.2.
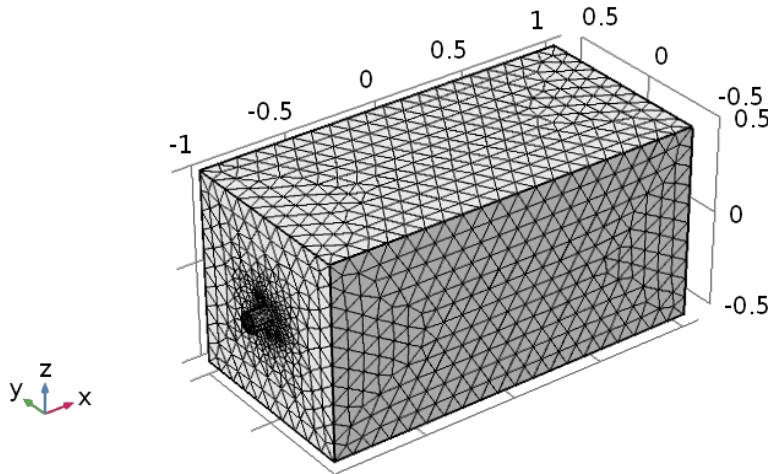

Figure 4.2: Example of how the mesh of the container looks like on the outside of the container when divided in mesh elements of tetrahedral shape. The mesh size in this figure is the predefined "coarse" mesh in Comsol.

Within Ekman boundary layers at the horizontal boundaries of the container, the vertical gradients are much larger than the horizontal as mentioned in section 2.4. By using the tetrahedral mesh elements in the boundary layer, the resolution in the z-direction is too coarse to accurately capture the vertical gradients. Hence, we use a different mesh next to the boundaries than in the rest of the container. The mesh at the horizontal boundaries consists of 15 mesh layers covering almost twice the thickness of the boundary layer. The geometry of a mesh element in the boundary layer is a prism. A side view of the mesh in the boundary region is shown in Figure 4.3, where we zoomed in on the bottom boundary layer.
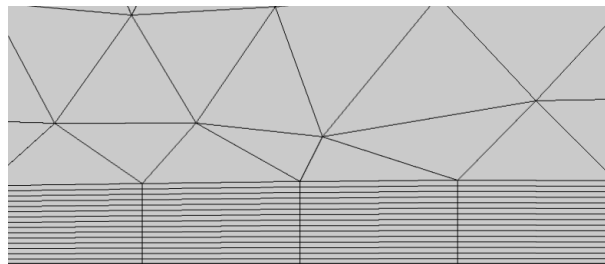

Figure 4.3: Close up of the side view of the mesh at the bottom boundary. The mesh elements in the boundary layer are prisms. At the boundary, the resolution of the mesh in the z-direction is much higher in the z-direction than in the bulk.

The density of the mesh, i.e. the resolution, in the interior is also of importance in the solution of the problem. The higher the density of the mesh, the more detailed results will be, and thereby, more realistic. However, the higher the density of the mesh, the longer the computation time will be. If the mesh size is fine enough, it is expected that the results of the simulation converge to the same results as for meshes with a higher density. To calculate the simulation in an acceptable time, we need to find a mesh size that allows this calculation time, and yields high enough accuracy to be comparable to experiments. One of the finest meshes preprogrammed in Comsol, the "finer" mesh, is used. In this case, one simulation ran for approximately one week in a Dell precision tower 7910 work station with two Intel® Xeon® CPU E5-2697 v3 2.60 Hz processors and a RAM of 128 GB. This computation time is too long for us because we want to compute simulations for several flow and rotation rates. This is why these results are used as a benchmark to find a mesh with a shorter computation time but whose results converge reasonably well to the results from the finer mesh. Following on this, two preprogrammed mesh sizes, "normal" and "fine", are compared to the finer mesh. The simulations with different meshes are compared using the outflux of the container with and without rotation. The outflux in time for the normal, fine and finer mesh are shown in Figure 4.4.
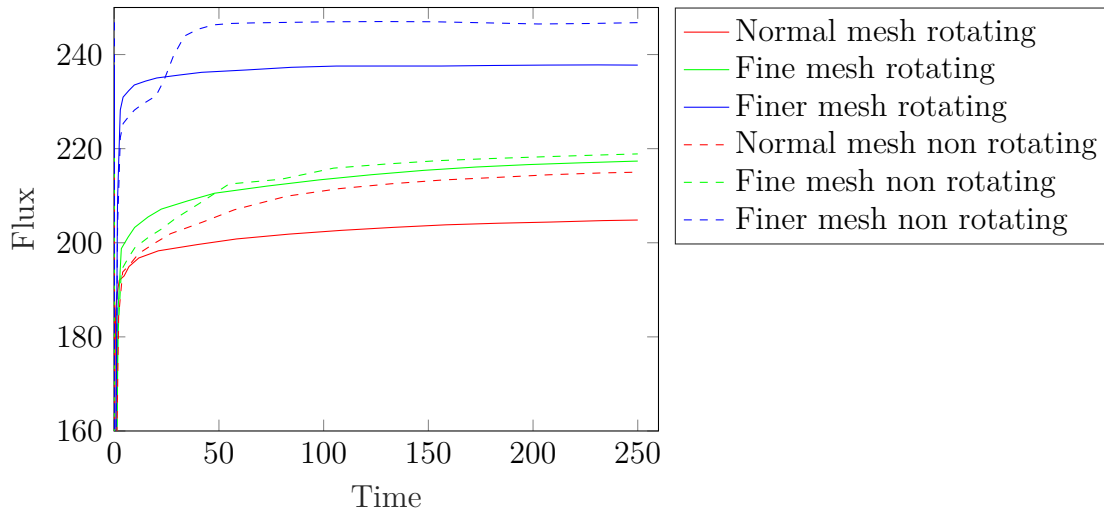

Figure 4.4: Comparison of the volume fluxes as function of time with and without rotation for the preprogrammed meshes in Comsol: normal, fine and finer.

From the data in Figure 4.4, the relative difference from the normal and fine mesh to the finer mesh are calculated as percentage of the finer mesh with and without rotation. The calculated differences are shown in Table 4.1. The normal mesh is found to deviate too greatly from the flow in the finer mesh. The fine mesh gets closer with rotation to the finer mesh but without rotation the flux is almost 12 % off from the finer mesh, which is comparable to the normal mesh. To get a trustworthy result within a reasonable calculation time, a mesh size is customized in between the mesh sizes of fine and finer. In Comsol the specified element size parameters set for this mesh are 0.045 for the maximum element size, 0.007 for the minimum element size, 1.115 for the maximum element growth rate, 0.45 for the curvature factor and 0.85 for the resolution of narrow regions. The results with the "custom" mesh are shown in Figure 4.5 with the fine and finer mesh. The results from the custom mesh lies closer to the finer mesh than the fine mesh. With rotation the difference is 2.4 % and without rotation 3.6 %. The custom mesh is still

within reasonable calculation time and approaches the results from the finer mesh and is therefore used to perform the simulations with.

Table 4.1: Difference in the flow rate compared to the finer mesh in % of the finer mesh with and without rotation.

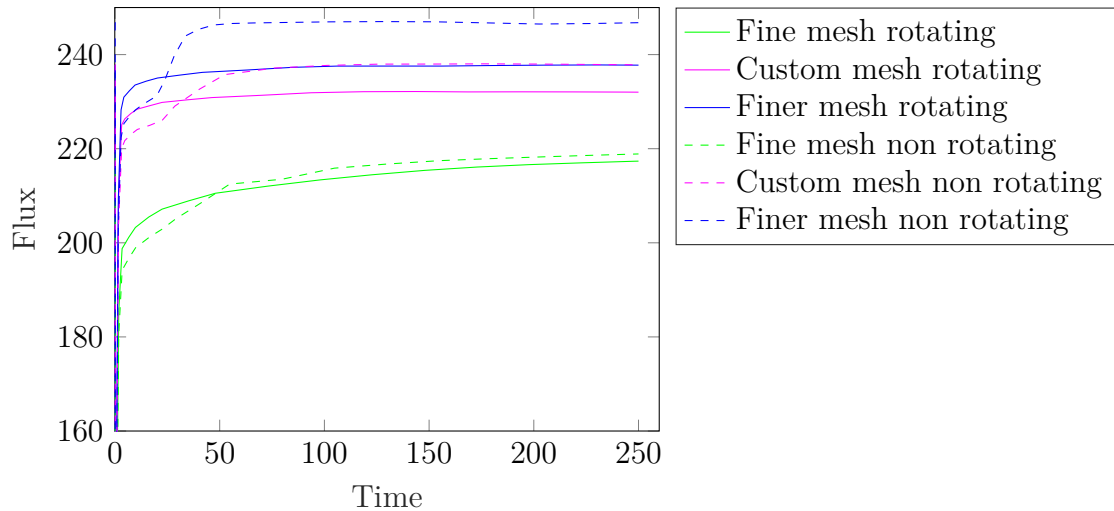| Mesh size	Difference with rotation [%]	Difference without rotation [%]
Normal	13.8	12.8
Fine	8.5	11.3

Figure 4.5: Comparison of the volume fluxes as function of time with and without rotation for the meshes in Comsol: fine, custom and finer.

4.3 Parameter values

4.3.1 Ekman number

To include rotation in the model, the Coriolis and centrifugal forces are added to the model as described in section 4.1. In the non-dimensional Navier-Stokes equation (4.5), the Coriolis force scales with E^{-1} and the centrifugal force with E^{-2}. The x, y and z-components for the Coriolis force the are given by

$$F_{cor,x} = 2vE^{-1}, \tag{4.8}$$
$$F_{cor,y} = -2uE^{-1}, \tag{4.9}$$
$$F_{cor,z} = 0. \tag{4.10}$$

The x, y and z-component for the centrifugal force are given by

$$F_{cent,x} = \sqrt{x^2 + y^2} \cos\left(\arctan(\frac{y}{x})\right)E^{-2}, \tag{4.11}$$

$$F_{cent,y} = \sqrt{x^2 + y^2} \sin\left(\arctan(\frac{y}{x})\right)E^{-2}, \tag{4.12}$$

$$F_{cent,z} = 0. \tag{4.13}$$

To determine the value of the Ekman number that corresponds to a rotation rate in the experiments, we calculate this value for that specific rotation rate. For example, for a $\Omega = 5$ rad/s, $\nu = 10^{-6}$ m^2/s and $L = 0.1$ m:

$$E = \frac{\nu}{\Omega L^2} = \frac{10^{-6} \cdot 2\pi}{0.1^2 \cdot 5} = 7957. \tag{4.14}$$

Rotation rates from 1 to 6 rad/s give corresponding Ekman numbers values from $E = 1591$ to 9549.

4.3.2 Pressure difference and the Reynolds number

The value P_0 is used to impose a pressure difference between the inlet and the outlet to force the flow. To determine which pressure corresponds to a certain flow rate in the experiments, the average Reynolds number in the center of the container is computed. The Reynolds number is given by

$$Re = \frac{UL}{\nu}, \tag{4.15}$$

where U is the flow velocity averaged over the plane $x = 0$. For a flow rate of 1.59 l/min in the experiment (with $\nu = 10^{-6}$ m^2/s and $L = 0.1$ m), $Re = 265$. Through trial and error, we obtained the dimensionless pressure $P_0 = 1.85 \cdot 10^9$ corresponding to $Re = 265$ in the center of the container.

Finally we make sure that the duration of the experiments and the simulations are the same. The length of an experiment T is 250 s. This means that the dimensionless time T', in other words, the length of the simulation should be

$$T' = T\frac{\nu}{L^2} = 25s0 \cdot \frac{\nu}{L^2} = 2.5 \cdot 10^{-3}. \tag{4.16}$$

For the pressure measurements in the experiments a sample rate of 100 Hz is used, for the simulations the results are saved with 10 Hz.

Chapter 5

Results and discussion

In this chapter, we present and discuss the effect of rotation on the measured flow rate, the flow pattern obtained from qualitative visualization and the measured pressure. We compare these findings with the results of the simulations.

5.1 Orientation and reliability of the pump

We aim to measure the effect of rotation on the flow rate through the container. Hence, the pump itself should not be affected by the rotation. Since the pump operates via a rotor, we speculate that it might be affected by the rotation of the table. To test this hypothesis, we measure the flow rate for different orientations for the pump. Firstly, we oriented the pump in the xy-plane in the center of the table and secondly in the xz-plane. In the ideal situation, the direction of the rotation should not matter since the setup is symmetrical. The results from the pump oriented in the xy-plane can be found in Figures 5.1(a) and 5.1(b) for clockwise and counterclockwise rotation of the table, respectively. Here, the measured signal of the flow rate is averaged over time. The figures show the change in the flow rate ΔQ as function of the rotation rate and the flow rate without rotation Q_{nr}. These measurements are performed at a constant voltage on the pump of 5.4 V. However, in these figures the flow rates on the y-axis are not constant because the output flow rate varies for a constant applied voltage. Hence, the average flow rates are different for each measurement. As can be seen by comparing Figures 5.1(a) and 5.1(b), the flow rate decreases when the table rotates in clockwise direction and increases when it rotates in the counterclockwise direction. From this, we see that the direction of rotation affects the pump.
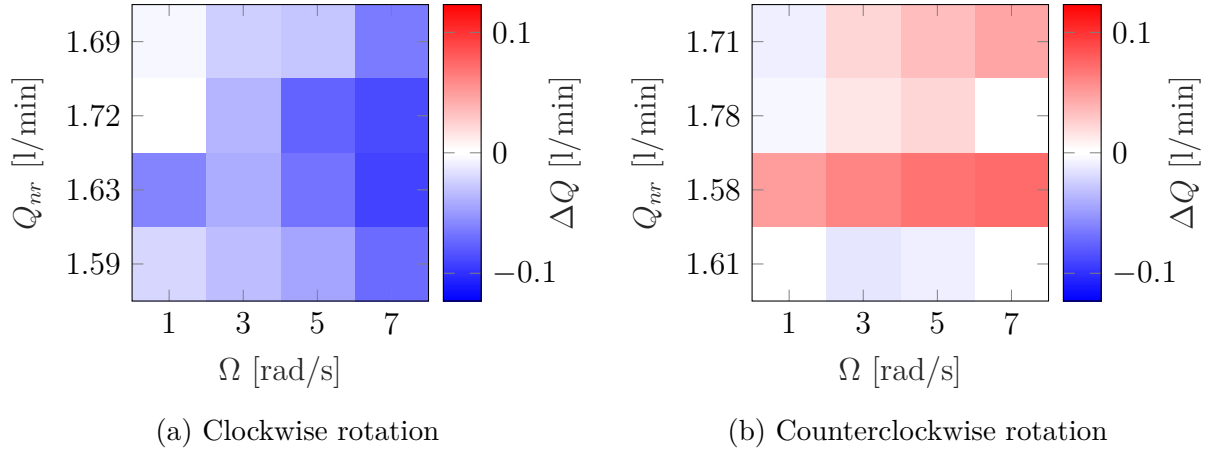
(a) Clockwise rotation

(b) Counterclockwise rotation

Figure 5.1: Change in the flow rate ΔQ as a function of the rotation rate Ω and the flow rate without rotation Q_{nr}. The pump is oriented in the xy-plane. (a) Shows the results with clockwise rotation and (b) the results with counterclockwise rotation.

The results from the pump oriented in the xz-plane are shown in Figures 5.2(a) and 5.2(b) for the clockwise rotation and counterclockwise rotation of the table, respectively. The figures show the change in the flow rate ΔQ as function of Ω and Q_{nr}. These figures show that the throughflow decreases for increasing rotation independently of the direction of rotation. This indicates that the pump is not dominated by rotation. Therefore, the pump was placed in the center of the table oriented in the xz-plane for all remaining experiments to diminish the effects of the rotation on the pump.

(a) Clockwise rotation
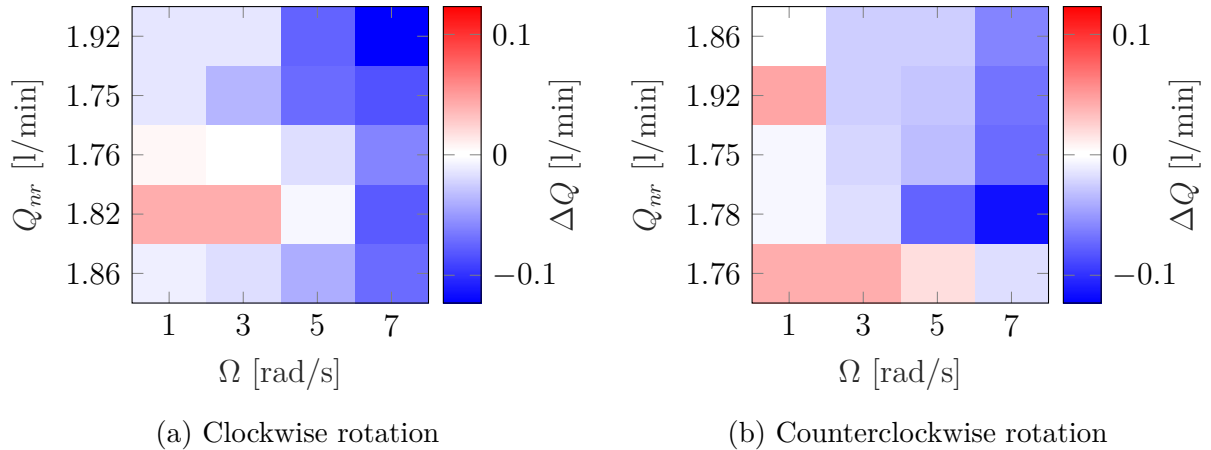
(b) Counterclockwise rotation

Figure 5.2: Change in the flow rate ΔQ as a function of the rotation rate Ω and the flow rate without rotation Q_{nr}. The pump is oriented in the yz-plane. (a) Shows the results with clockwise rotation and (b) the results with counterclockwise rotation.

The experiment is repeated several times, to check the reliability and reproducibility of the experiment. However, the reproducibility is limited as was observed by the fact that a constant applied voltage to the pump corresponds to various flow rates, as observed in the y-axis of Figures 5.1 and 5.2. We performed a test by measuring the flow rate continuously for almost a full day. We have observed large variability in the signal from this measurement, which might explain the inconsistencies. In Figure 5.3, we show a part of this measurement where the pump ran continuously for 60 minutes on a constant voltage of 5.4V. It was expected that the flow rate would remain constant and that no large fluctuations would be present. Unfortunately, as shown in Figure 5.3, there are large fluctuations present in the flow rate: the average flow rate is 1.78 l/min, with a maximum of 2.05 l/min and a minimum of 1.64 l/min and a standard deviation $\sigma = 0.07$ l/min. This gives a total difference of 0.41 l/min between the maximum and minimum flow rate corresponding to a relative fluctuation of 23% as compared to the average flow. To compute the effect of rotation, the flow rate in each experiment was averaged over 150 s. It is clear from Figure 5.3, that this time span is not enough to average out this large fluctuations in the flow throughput due to the jumps that are present.
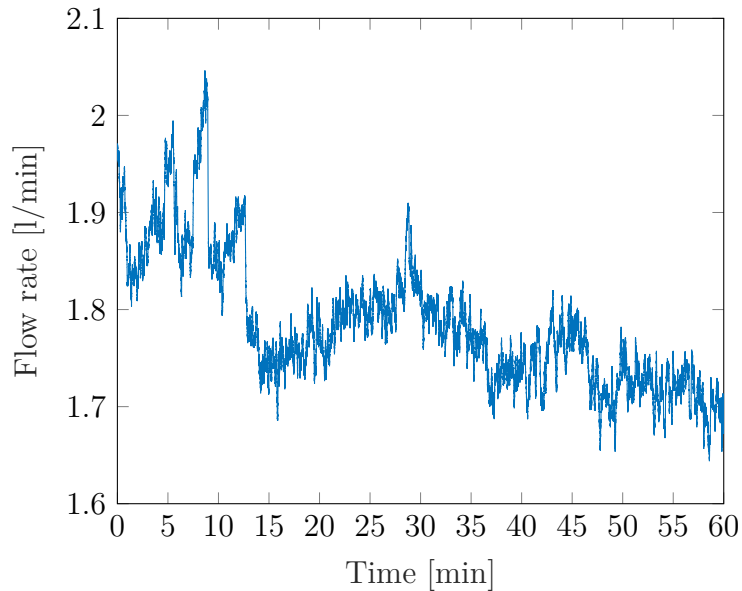

Figure 5.3: Flow rate at a constant input voltage of 5.4 V on the pump without rotation as a function of time for one hour.

5.2   Effect of background rotation on the flow rate

In the experiments, we have measured the difference in flow rate for a nonrotating and a rotating case. Figure 5.4 shows change in the flow rate ΔQ as a function of the rotation rate Ω for different values of the nonrotating flow rate Q_{nr}.
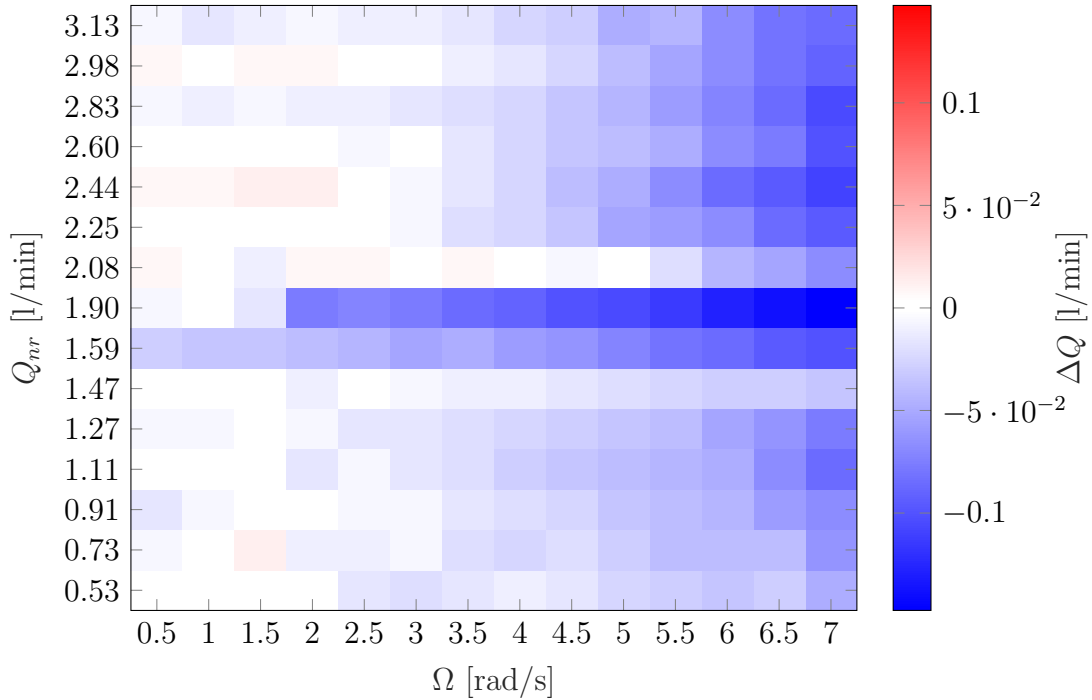
Figure 5.4: The change in the flow rate ΔQ as a function of the rotation rate Ω for different values of Q_{nr}.

In general, the flow rate decreases for increasing rotation rate. The overall decrease with increasing rotation rates is in agreement with the results from previous numerical simulation [13] and in disagreement with previous experiments [3]. The few measurements where an increase in the flow rate was observed (such as at 2.44 l/min and 0.5 to 2.5 rad/s) are small increases. They might be the result of fluctuations of the pump throughput as discussed in section 5.1. As can be seen in Figure 5.4, the flow rates of 1.90 and 1.59 l/min have a sharper decrease than the surrounding flow rates. This behavior may also be caused by the unreliable behavior of the pump. When the pump jumps to a different flow rate during rotation, the error can be significant if the jump occurs between two measurements. In order to check whether this is a property of the flow or caused by the pump, the experiments were repeated for selected values of Ω and the flow rate.

Figure 5.5(a) shows the results from Figure 5.4 for the selected experiments and Figure 5.5(b) shows the repeated experiments. Each bin represents the change in the flow rate ΔQ as a function of the rotation rate for different values of the nonrotating flow rate. For the original experiments, the decrease is suddenly stronger compared to the surrounding flow for $Q_{nr} = 1.59$ l/min. For the repeated experiments, this behavior is not present. It is plausible that the fluctuations in the pump are causing the inconsistent results in Figure 5.4. For the repeated experiments with the highest flow rate (3.15 l/min), we find an increase in the flow rate for the smallest rotation rates. This is not in agreement with the original measurements in Figure 5.5(a) with 3.13 l/min, where the flow is inhibited for these rotation rates. The same goes for the relatively large changes in the flow rate for 7 rad/s for 2.80 and 2.43 l/min. All these differences are most likely caused by the unreliability of the pump. The changes in the flow rate are at most 9% of the nonrotating flow rate and therefore, very susceptible to the fluctuations in the pump. In spite of the differences, the decrease ΔQ for increasing rotation rate is consistent for

34

both sets of experiments. The overall decrease in the flow rate with increasing rotation rates is partly explained by the energy that is needed for sustaining the Ekman layer, Ekman fluxes and the energy that is needed to support the secondary flow, generated by the Coriolis force [4, 7]. This leads to a pressure drop which causes the decrease of the throughflow.
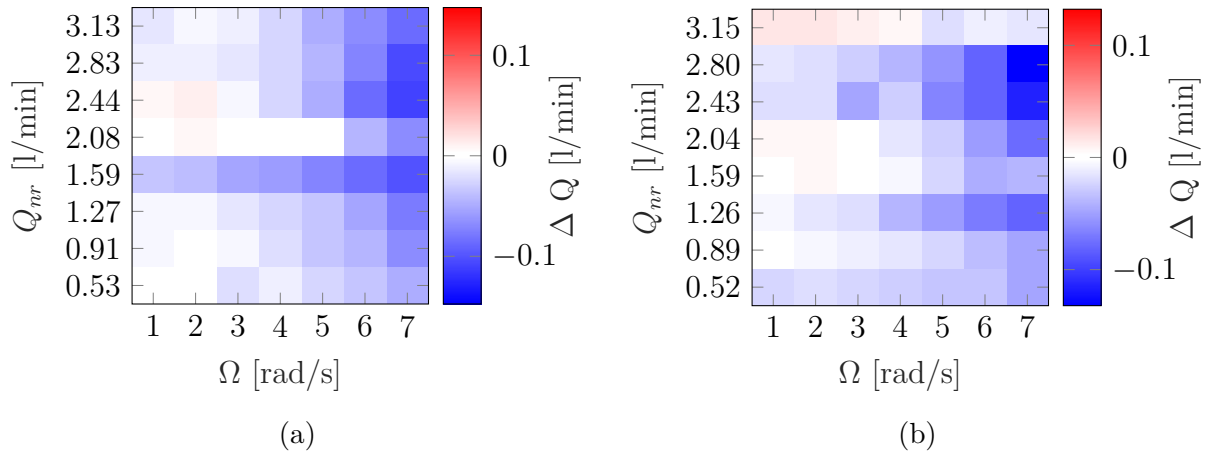

Figure 5.5: Change in the flow rate ΔQ as a function of the rotation rate Ω for different values of the nonrotating flow rate Q_{nr}: (a) results coming from the original set of experiments shown in Figure 5.4 and (b) results from the repeated experiments.

To get more insight into the flow and the reliability of the data, the experiments are compared to the simulations. The applied voltage of 5.4 V on the pump is chosen. This voltage generates a $Q_{nr} = 1.59 \pm 0.07$ l/min for the experiments. In the simulations, the corresponding dimensionless pressure $P_0 = 1.85 \cdot 10^9$. In Figure 5.6, the relative change in flow rate ΔQ_{rel} as function of the rotation rate is shown for the experiments and simulations. The change in flow rate $100\% \cdot (Q_r - Q_{nr})/Q_{nr}$ where Q_r is the flow rate with rotation. The error bars in the experimental data represent the standard deviation in the measured signal averaged over 150 s per rotation rate.

Between the rotation rates 0 and 1 rad/s the flow rate decreases for the simulations. From 1 to 6 rad/s, the change in flow rate is still negative, but to a smaller extent in the range of -4.9 to -2.2%. In the range from 1 to 6 rad/s, this behavior in the simulations is the inverse from the results from the experiments where the difference in the flow rate decreases as the rotation rate increases. Apart from the range in which the differences in flow rates are present, there is no qualitative agreement between the simulations and experiments. These differences might be caused by the compromise made in the computation time and mesh size in the simulations, i.e. the mesh size is not fine enough to obtain a reliable result. Besides this, the difference might as well be explained by problems in the experiments due to the unreliabilities in the behavior of the pump.

The relative change in the flow rate ΔQ_{rel} can be calculated for the different meshes from section 4.2 for simulations with $\Omega = 5$ rad/s. The results of this calculation are shown in Table 5.1. The custom mesh size is used for the results shown in Figure 5.6. The value of ΔQ_{rel} for the fine mesh deviates more from the experimental obtained flow difference of -4.37 %. However, the finer mesh is closer to the obtained flow difference from the experiments. Hence, we see that the mesh size is not fine enough to perform

accurate simulations.

Table 5.1: Relative flow rate difference ΔQ_{rel} for the fine, custom and finer mesh size for a rotation rate of 5 rad/s and $P_0 = 1.85 \cdot 10^9$. The custom mesh is used to compare the simulations to the results in Figure 5.6.

Mesh size	ΔQ_{rel} [%]
Fine	-0.70
Custom	-2.46
Finer	-3.58
Experiment	-4.37

The behavior in the simulations is self-consistent since the difference in the flow rate decreases to zero for small rotation rates. However, the results of our numerical simulations are not in agreement with previous simulations [13]. Their results are in better agreement with our experimental results, which indicates that our numerical simulations are indeed not accurate enough.
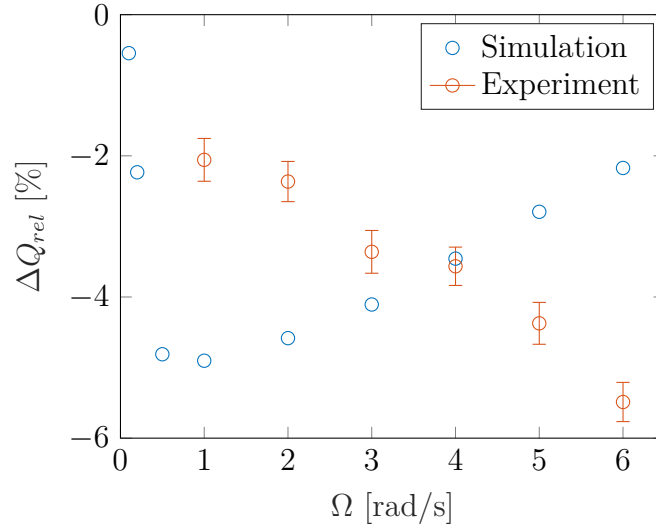

Figure 5.6: The relative change in the flow rate ΔQ_{rel} as a function of Ω for $Q_{nr} = 1.59$ l/min for the experiments and simulations. The error bars in the experiments represent the standard deviation over the measured signal.

5.3 Flow structure

To get a better understanding of the behavior of the flow in the container, qualitative flow visualizations are performed. This is done for the same initial flow rate, as determined by a constant voltage on the pump as discussed in Chapter 3 which is 1.59 ± 0.07 l/min. This visualization is performed in the xy-plane at two different heights. Firstly, at the center height, i.e. $z = 0$ in Figure 4.1 and secondly at 3/4 height of the container which equals $z = 0.25$. A background correction is applied to all frames to filter out all non-moving objects. Next, we construct the flow pattern by adding 100 frames. This allows us to reveal the flow pattern in the container in the xy-plane through the streaklines of particles in suspension. A more detailed discussion of the method can be found in appendix A.

Figure 5.7 shows the results of the flow pattern from the visualization at the center height for $\Omega = 0$ to $\Omega = 5$ rad/s. The rotation of the table is in the counterclockwise direction in the images. At $(x, y) = (0, 5)$ cm, the flow enters the container. In Figure 5.7(a) for $\Omega = 0$ rad/s, the flow travels towards the outlet at $(x, y) = (20, 5)$ cm in a straight line, and a flow in the negative x-direction is present in the top part of the figure. In Figures 5.7(b) to 5.7(f), as rotation is increased, the flow entering the container at $(x, y) = (0, 5)$ cm is bent towards the bottom of the figure. This deflection is due to the Coriolis force. In all figures with rotation, a large scale cyclonic circulation is visible above the bent flow. A cyclonic circulation flows in the same direction as the background rotation. A anticyclonic vortex is visible in the left, bottom corner of Figures 5.7(e) and 5.7(f). An anticyclonic vortex rotates in the opposite direction of the background rotation.

The flow patterns obtained from the visualization at 3/4 height of the container are shown in Figure 5.8 for $\Omega = 0$ to $\Omega = 5$ rad/s. The flow from the jet entering at the center height is not visible. In Figure 5.8(a), which is the visualization without rotation, there is no clear flow pattern visible. In Figures 5.8(b) to 5.8(f), where a background rotation is present, large scale cyclonic circulations are visible as at the center height in Figure 5.7. The anticyclonic vortex in the corner left below is also visible for $\Omega = 4$ and $\Omega = 5$ rad/s.
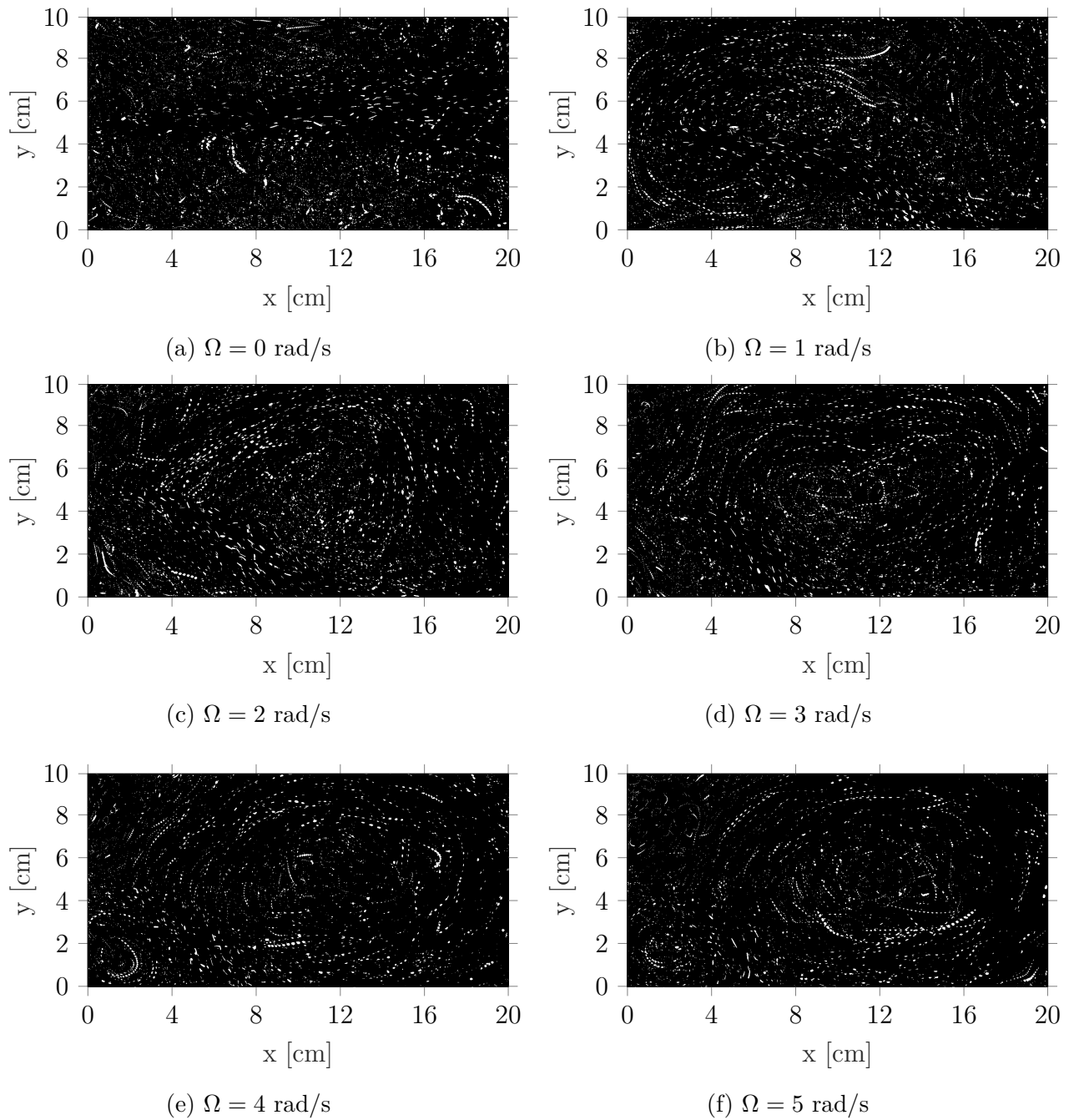
Figure 5.7: Flow patterns at the center height made visible by streaklines of suspended particles in the container for different rotation rates between 0 and 5 rad/s. These images are obtained by superposition of 100 images spanning 3.0 s. The rotation direction of the table is counterclockwise. The flow enters the container at $(x, y) = (0, 5)$ cm. In the figures with rotation (b) to (f), the flow is bent due to the Coriolis force towards its right. In these figures a large scale cyclonic circulation is visible. In (e) and (f) an anticyclonic vortex is present in the corner left below.

(a) $\Omega = 0$ rad/s

(b) $\Omega = 1$ rad/s

(c) $\Omega = 2$ rad/s

(d) $\Omega = 3$ rad/s

(e) $\Omega = 4$ rad/s
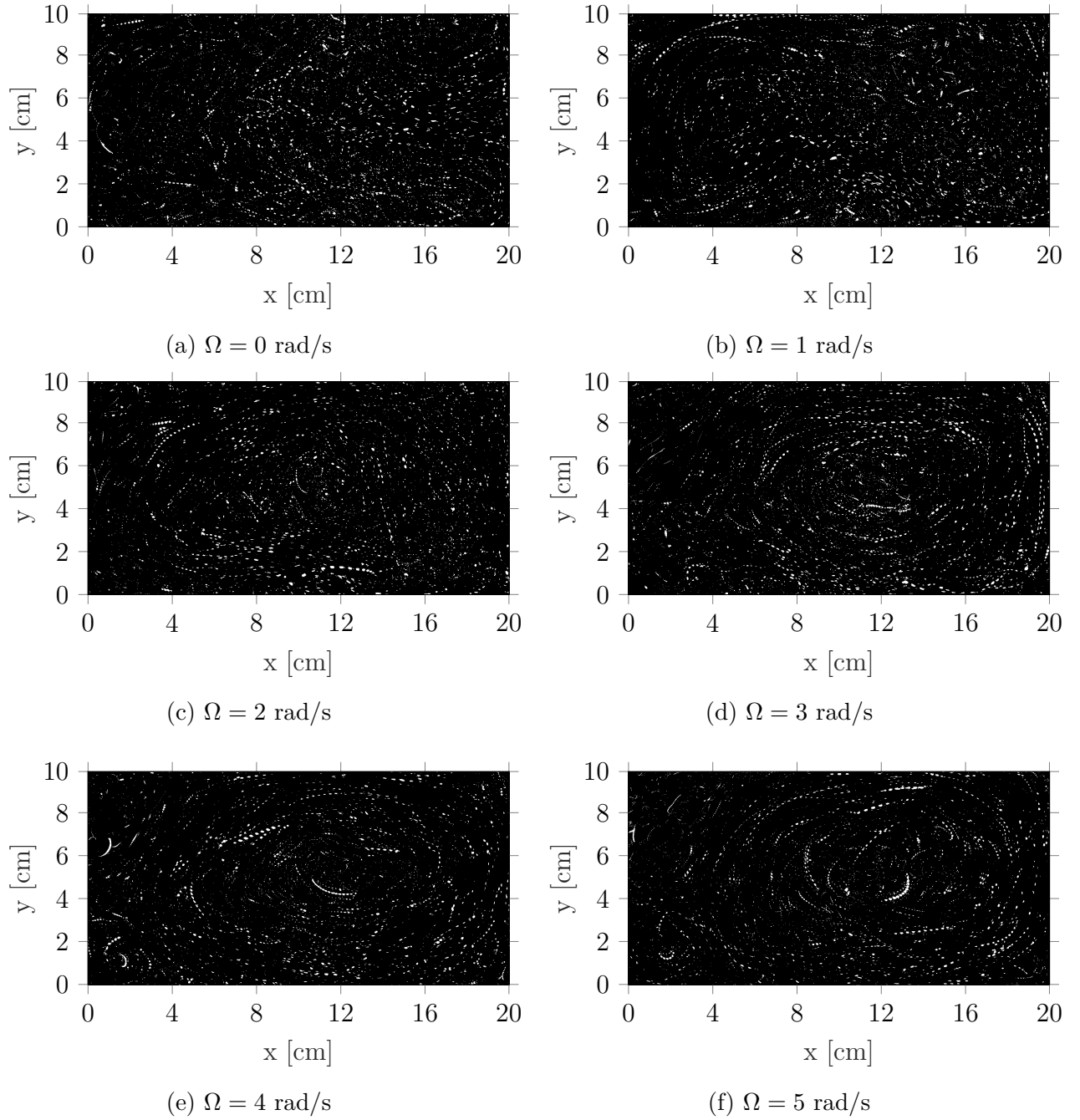
(f) $\Omega = 5$ rad/s

Figure 5.8: Flow pattern at 3/4 height made visible by streaklines of suspended particles in the container for different rotation rates between 0 and 5 rad/s. The rotation direction of the table is counterclockwise. These images are obtained by superposition of 100 images spanning 3.0 s. The flow enters the container at $(x, y) = (0, 5)$ cm. In the figures with rotation (b) to (f), the flow is bent due to the Coriolis force towards its right. In these figures a large scale cyclonic circulation is visible. In (e) and (f) an anticyclonic vortex is present in the corner left bottom. Orifice 5 and 6 are respectively present at $(0.35, 9.3)$ and $(0.35, 0.7)$ cm.

From the simulations, two-dimensional streamlines are obtained in the xy-plane by setting the vertical velocity $w = 0$. Figures 5.9 and 5.10 show the streamlines from the simulations at the center height and 3/4 height, respectively. The nonrotating flow rate $Q_{nr} = 1.59$ l/min, and the rotation rates range from 0 to 5 rad/s. The axis of these figures are scaled to the dimensions of the container in cm. The inlet of the container is at $(x, y) = (0, 5)$ cm and the outlet at $(x, y) = (20, 5)$ cm at the center height of the container.

Experiments and simulations are compared by comparing Figure 5.7 to Figure 5.9. The flow travels straight from the inlet towards the outlet without being bent in both the experiments and simulations for $\Omega = 0$ rad/s. In the simulations vortices are present in the corners. In the experiment, a vortex can be seen in the right bottom corner but in the other corners, no vortices are present. In the streamlines in the simulations with rotation (Figure 5.9(b) to 5.9(f)), the flow is bent due to the Coriolis force as was also seen in the visualization of the experiments. However, the flow is bent less strongly in the simulations. This might be caused by the chosen mesh size. When the flow velocity in the simulation is not the same as in the experiments, the Coriolis force will also deviate. In the figures with rotation the large scale cyclonic circulation is seen in the simulations as was in the experiments and seems stronger present for the three highest rotation rates in the simulations. A vortex in the lower left corner is present for $\Omega = 4$ and $\Omega = 5$ rad/s in the experiments. In the simulations for $\Omega = 4$ and $\Omega = 5$ rad/s (Figure 5.9(e) and 5.9(f)), a vortex is present below the bent jet. The position of the center and the diameter of the vortex is different in the simulations compared to the experiments which might again be due to the chosen mesh.

At 3/4 height, Figure 5.8 is compared to Figure 5.10. In neither the experiments nor the simulations, the jet that is entering at the center height of the container is visible. In the simulations for $\Omega = 0$ rad/s, the vortices present at the center height are still visible. In the experiments, no clear structures or vortices are visible. In the experiment for $\Omega = 1$ rad/s, a circulation is present on the left. In the simulations this circulations is present as well, as seen in Figure 5.10(b). However, in the simulation, a lot of vortices are present and more circulations which are not visible in the experiments. A large scale cyclonic circulation is present in the experiments and simulations for $\Omega = 2$ to $\Omega = 5$ rad/s. The centers of the circulation are not at the same position in the simulations and experiments but this might be due to the used mesh size. The vortex in the corner left below in the experiments for rotation rates of 4 and 5 rad/s is not seen in the simulations as can be seen in Figure 5.10(e) and 5.10(f). However, a vortex is present in the simulations for both rotation rates at approximately $(x, y) = (10, 2)$ cm which is not present in the experiments.
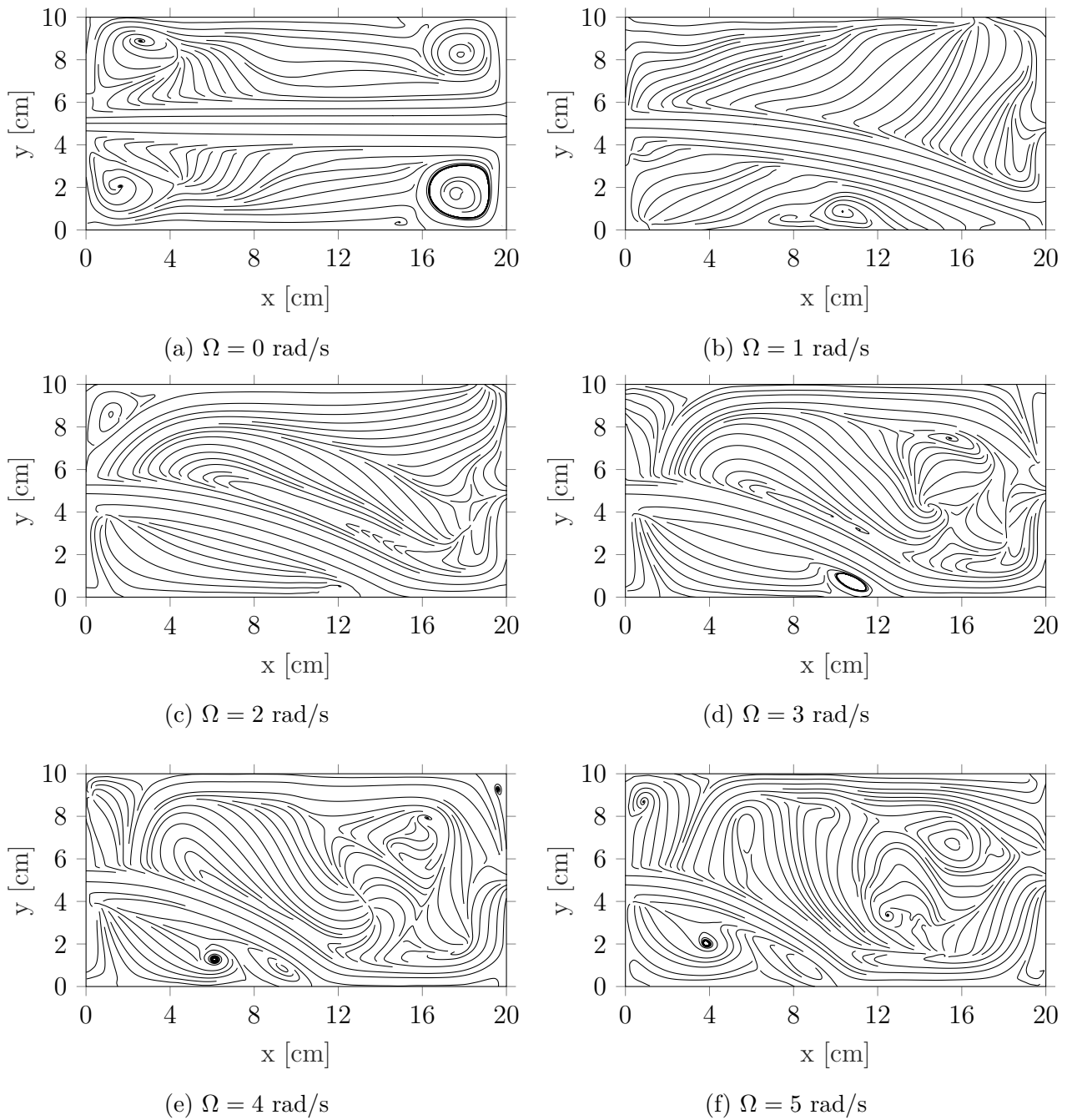
Figure 5.9: Two-dimensional streamlines at the center height ($z = 0$) from the simulations for rotation rates between 0 and 5 rad/s. Streamlines obtained by setting $w = 0$. The rotation direction of the table is counterclockwise. The flow enters the container at $(x, y) = (0, 5)$ cm.
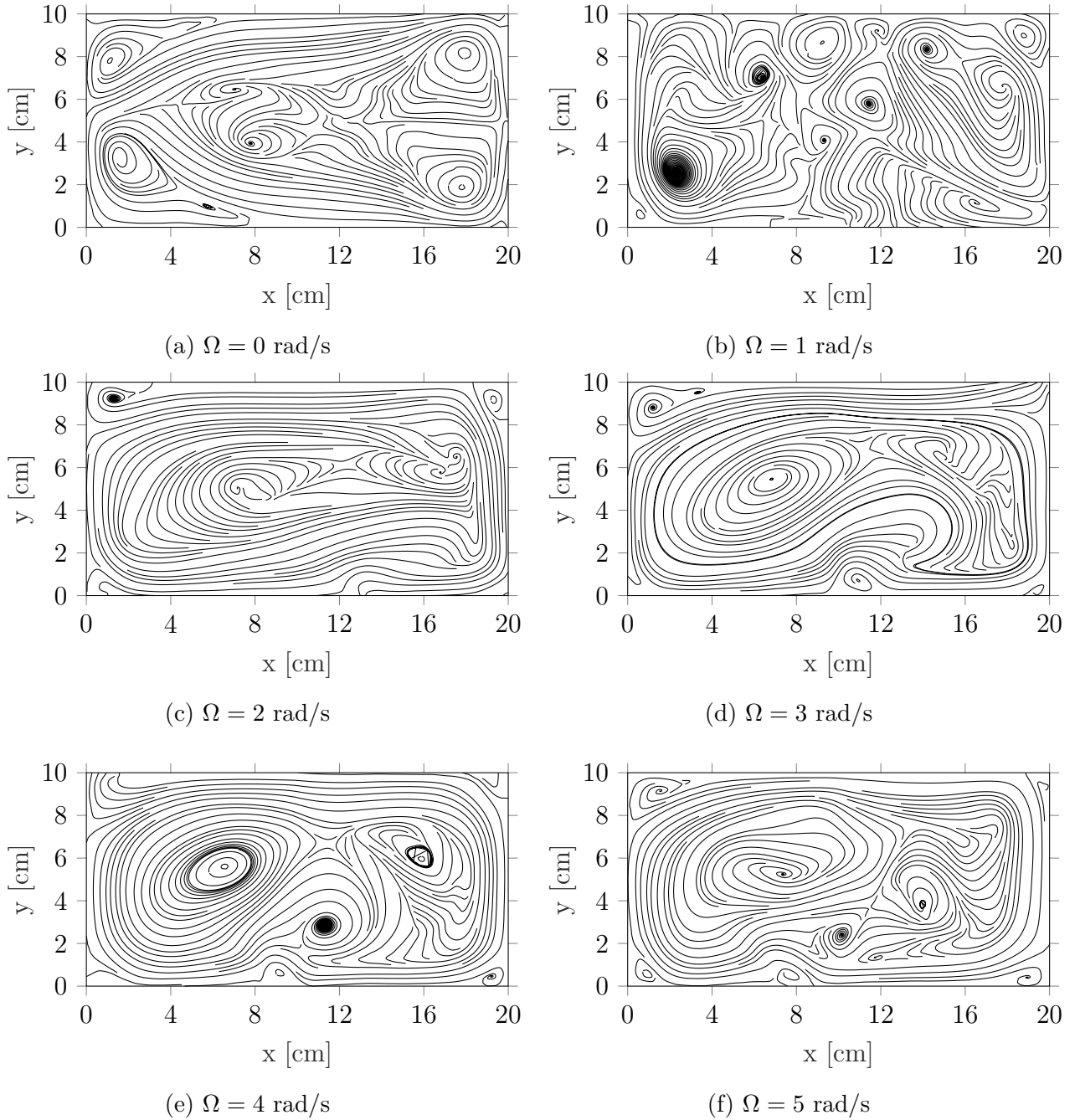
Figure 5.10: Two-dimensional streamlines at 3/4 height ($z = 0.25$) from the simulations for rotation rates between 0 and 5 rad/s. Streamlines obtained by setting $w = 0$. The flow enters the container at $(x, y) = (0, 5)$ cm at the center height and is not visible here.

5.4 Mean cross-channel pressure difference

In the rotating container, the flow can be in geostrophic balance as discussed before in section 2.1. To determine whether the flow is in geostrophic balance, the pressure difference ΔP_{5-6} between orifice 5 and 6 is measured. The positions of orifices 5 and 6 are shown in Figure 3.2. The pressure difference is averaged over the length of the signal

which equals 150 s. The average magnitude of this signal is shown in Figure 5.11. The pressure differences corresponding to the nonrotating flow rates equal to 3.13 and 2.98 l/min at $\Omega = 2$ to $\Omega = 6$ rad/s exceed the limit of -25 Pa of the pressure meter. Hence, the actual pressure difference could not be measured.

The flow is bent towards orifice 6 due to the Coriolis force. Therefore, it is expected ΔP_{5-6} to be negative for strong rotation rates. This is observed in the triangular regions on the top left part and in top right part of Figure 5.11. These two regions with a negative pressure difference are separated by an upward sloping line indicated in orange/red colors. This sloping line represents a sudden jump in the pressure difference and corresponds to a local Rossby number $Ro = 1$. The Rossby number $Ro = U/(fL)$ gives the ratio between inertial forces and the Coriolis force. When $Ro > 1$ inertial forces dominate [3]. This is associated with the area on the left side of the sloping line in Figure 5.11. When $Ro < 1$, the Coriolis force dominates, inertial waves can be present, and the flow is assumed to be geostrophic. The area on the right of the sloping line is associated with the $Ro < 1$ regime.

The pressure difference is overall positive for low flow rates. In section 5.3 an anticyclonic vortex is seen in the left bottom corner for high rotation rates. Since orifice 6 is located above this vortex, it might affect the measured pressure difference ΔP_{5-6} resulting in a positive pressure difference for high rotation rates.
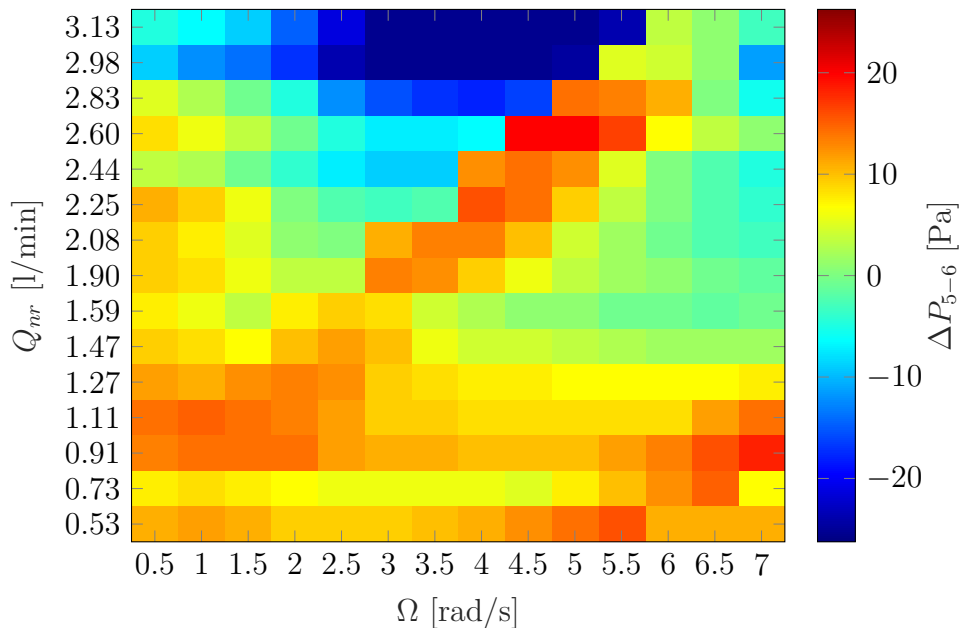

Figure 5.11: Cross-channel pressure difference ΔP_{5-6} between orifice 5 and 6 as function of Ω and Q_{nr}. The pressure differences for the nonrotating flow rates equal to 3.13 and 2.98 l/min at $\Omega = 2$ to $\Omega = 6$ rad/s are smaller than -25 Pa of the pressure meter.

The reproducibility of the pressure measurements is tested by repeating the experiment for selected values of Ω and flow rates. Figure 5.12(a) shows the results from Figure 5.11 for the selected experiments and Figure 5.12(b) shows the repeated experiments. Each bin represents again the cross-channel pressure difference over orifice 5 and 6 (ΔP_{5-6}) as a function of Ω and different values of Q_{nr}. The separation of the two regimes with the $Ro = 1$ line is still visible and is present in approximately the same place. Where $Ro > 1$,

we have a negative pressure difference for the large flow rates in both figures. Again for the flow rates of 3.13 l/min in (a) and 3.15 l/min in (b) for $\Omega = 3$ to $\Omega = 6$ rad/s the pressure difference exceeded the range of the pressure meter and is, thereby, not properly represented. On the right of $Ro = 1$ the pressure difference is slightly negative in both figures. In the bottom part of the figures, we see an increase in the pressure difference for the lowest three flow rates. There are significant differences in the measured pressure difference for the flow rates of 1.27 l/min in Figure 5.12(a), 1.26 l/min in Figure 5.12(b) and 1.59 l/min in both figures. These differences could be the effect of a vortex that might be present under orifice 6 as was seen in the visualization of the flow in section 5.3. These fluctuations might also be influenced by jumps in the flow rate due to the pump. When the pump fluctuates, the flow in the container is not in steady state and the pressure can fluctuate. To see whether this is caused by the pump or by the effect of the vortex, the experiments should be repeated using a constant and reliable pump without fluctuations.
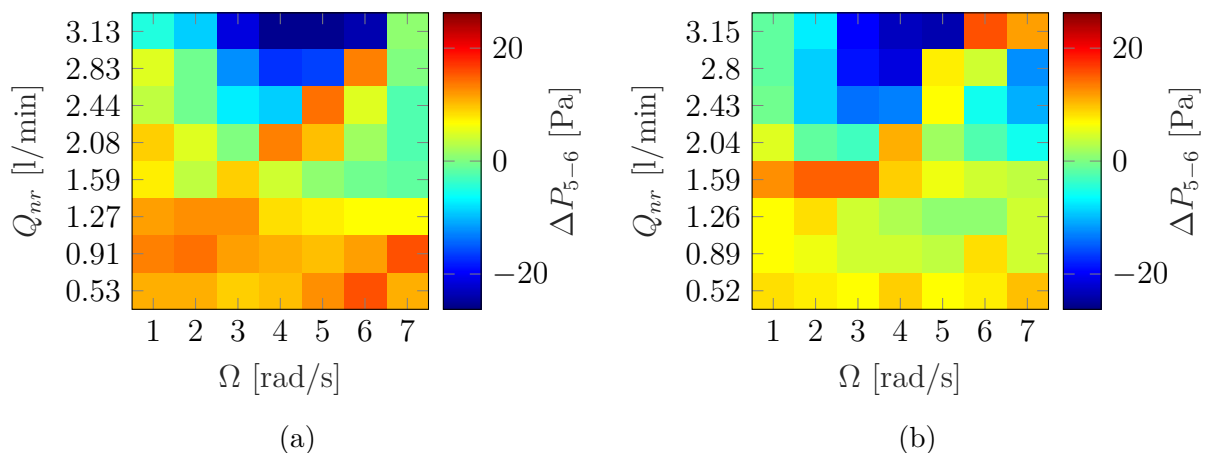

Figure 5.12: Pressure difference between orifice 5 and 6 (ΔP_{5-6}) averaged over 150 s for two sets of experiments. (a) Results coming from the original set of experiments shown in Figure 5.11, and in (b) results from the repeated measurements.

The results from the experiments are compared to the simulations. The voltage of 5.4 V applied on the pump is chosen, which generates $Q_{nr} = 1.59 \pm 0.07$ l/min. The pressure $P_0 = 1.85 \cdot 10^9$ is used in the simulations, corresponding to the same nonrotating flow rate. In section 4.1, we made the pressure dimensionless using $P_0 = -\Delta P L^2 / 2\rho\nu^2$. The pressure difference $\Delta P'_{5-6}$ from the simulations is made dimensionful using the inverse. In Figure 5.13(a), the cross-channel pressure difference ΔP_{5-6} as function of the rotation rate is shown for the experiments and simulations. The error bars in the experimental data represent the standard deviation in the measured signal averaged over 150 s. The error bars might not take large jumps or trends in the flow rate into account.

The pressure difference in the experiments is positive and increasing for rotation rates between 1 and 3 rad/s. From $\Omega = 3$ to $\Omega = 4$ rad/s, there is a sudden decrease in the pressure difference. After this jump the pressure difference decreases from 4 to 6 rad/s. The jump in the pressure difference from 3 to 4 rad/s indicates the transition to the inertial regime. Comparing this to the simulations, we observe that the pressure difference in the simulations is within the error bars of the experiments in the inertial regime. Figure 5.13(b) zooms in on the pressure differences in the simulations. The pressure difference in the simulations does not show the same increasing trend as the experiments for 1 to 3

rad/s. The pressure difference increases from 1 to 2 rad/s after which is makes step to a lower pressure difference for 3 rad/s. However, from 3 to 5 rad/s the pressure difference increases, and from 5 to 6 rad/s, a jump in the pressure difference is present. This jump might corresponds to the transition to the inertial regime, but to be certain, simulations for higher rotation rates should be added in the future.
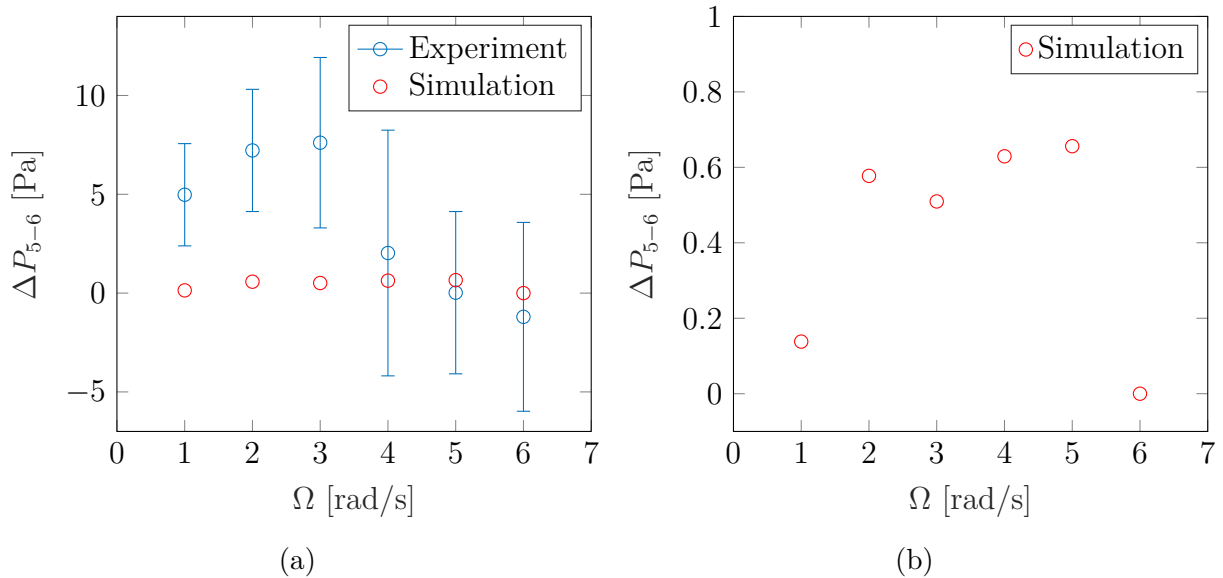

(a)

(b)

Figure 5.13: Cross-channel pressure difference ΔP_{5-6} as a function of Ω for $Q_{nr} = 1.59 \pm 0.07$ l/min for the experiments and simulations. The error bars in the experiments represent the standard deviation over the measured signal.

Similar pressure measurements to the ones used in Figure 5.11 had been performed presented in [3]. Those results are shown in Figure 5.14. In this figure, the cross-channel pressure difference over orifice 5 and 6 ΔP_{5-6} is plotted as a function of the rotation rate Ω for different values of the nonrotating flow velocity u. The flow velocity u is calculated from the flow rate Q such that $u = Q/(Hd)$, where $H = 0.1$ m the fluid height and $d = 0.005$ m the diameter of the tubing. To compare our measurements to those, we rescale our measurements from Figure 5.11 to m/s as shown in Figure 5.15. The equivalent domain in Figure 5.15 to Figure 5.14 is noted with the dashed area. In the results in Figure 5.14, the straight black line represents the local $Ro = 1$, the sloping blue lines represent the geostrophic equilibrium for fixed pressure differences ΔP_{5-6}.

In Figure 5.14 and 5.15, the pressure differences is positive in the $Ro > 1$ region and for the highest flow rates negative for the same flow velocities. The range of the pressure difference in Figure 5.14 is from -7 to 2 Pa which is in the same order of our results in the same flow range in Figure 5.15. In the region where $Ro < 1$, the pressure difference decreases for increasing flow velocities. In our measurements, a geostrophic flow is not seen at first sight which is present in Figure 5.14 as indicated with the blue lines. This might be because our flow range is a lot larger and the resolution in the rotation and flow rate is smaller than in Figure 5.14.
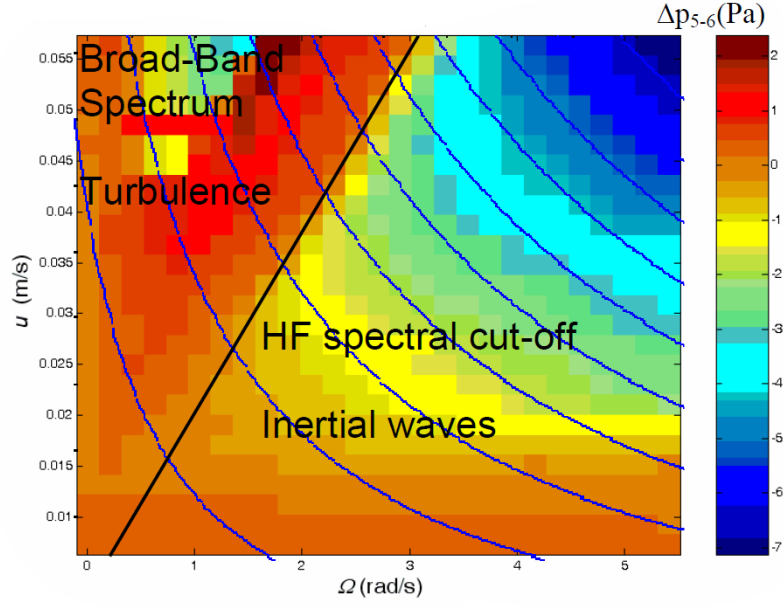
Figure 5.14: Cross-channel pressure difference over orifice 5 and 6 ΔP_{5-6} as function of the rotation rate Ω and the nonrotating flow velocity u from the measurements in [3]. The black line represents the local $Ro = 1$. The blue sloping lines represent the geostrophic equilibrium which for fixed lateral pressure gradient throughflow in inversely proportional to the rotation rate.
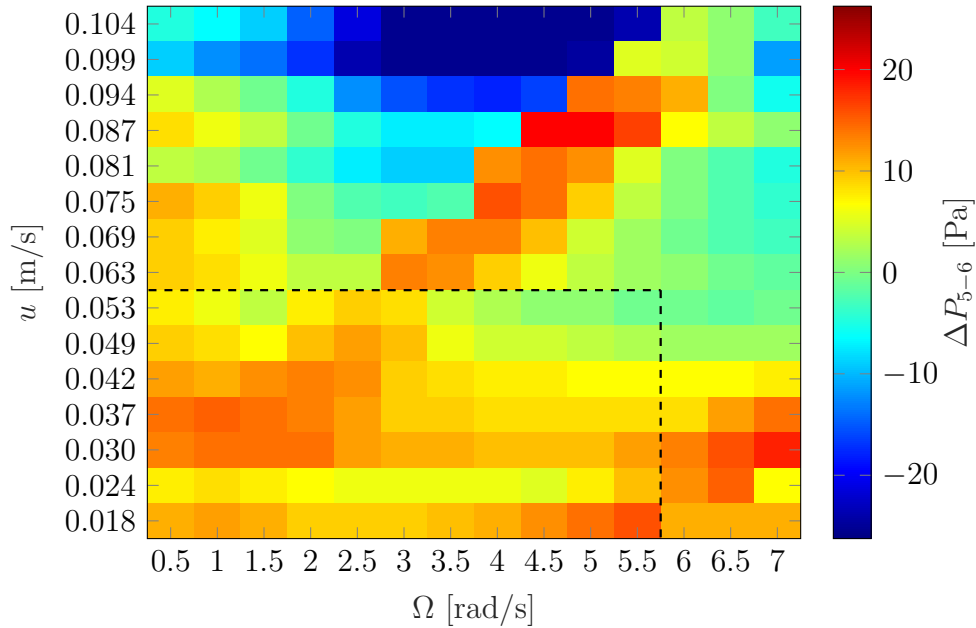

Figure 5.15: Cross-channel pressure difference ΔP_{5-6} between orifice 5 and 6 as function of Ω and the nonrotating flow velocity u. The pressure differences for $u = 1.04$ m/s and $u = 0.099$ m/s at $\Omega = 2$ to $\Omega = 6$ rad/s are smaller than -25 Pa of the pressure meter.

We assumed that the flow in the container is geostrophic which was not found in the measurements shown in Figure 5.15. To check the presence of geostrophy, the measured pressure differences from Figure 5.15 are divided by the flow velocity u as shown in Figure 5.16. Using the geostrophic balance from eq. (2.2) and (2.3), we can neglect eq. (2.3) since we measure the pressure difference in the y direction. This leaves

$$fu = -\frac{1}{\rho}\frac{\partial P}{\partial y} = -\frac{1}{\rho}\frac{\Delta P_{5-6}}{\Delta y}, \tag{5.1}$$

with ρ the constant density of the water, $f = 2\Omega$ the Coriolis parameter, ΔP_{5-6} the pressure difference over the orifice 5 and 6 and Δy the distance between orifice 5 and 6 which is constant. Rewriting this equation where the pressure difference is divided by the flow velocity gives

$$-\rho\Delta y 2\Omega = \frac{\Delta P_{5-6}}{u}. \tag{5.2}$$

Hence, in case of a geostrophic flow, $\Delta P_{5-6}/u$ should scale linearly with Ω. Figure 5.16 shows the linear increase with the rotation rate is only present for the lowest four flow rates from 0.53 to 1.10 l/min for rotation rates of 4.5 to 7 rad/s. Another way to check the presence of geostrophy is by dividing the pressure difference ΔP_{5-6} by $2\Omega u$. From eq. (5.2), we obtain a constant $\Delta P_{5-6}/2\Omega u$. This normalized pressure difference $\Delta P_{5-6}/2\Omega u$ is shown for the lowest four flow rates of 0.53 to 1.10 l/min in Figure 5.17. The geostrophic behavior is seen for these four flow rates for the high rotation rates of 6 to 7 rad/s.
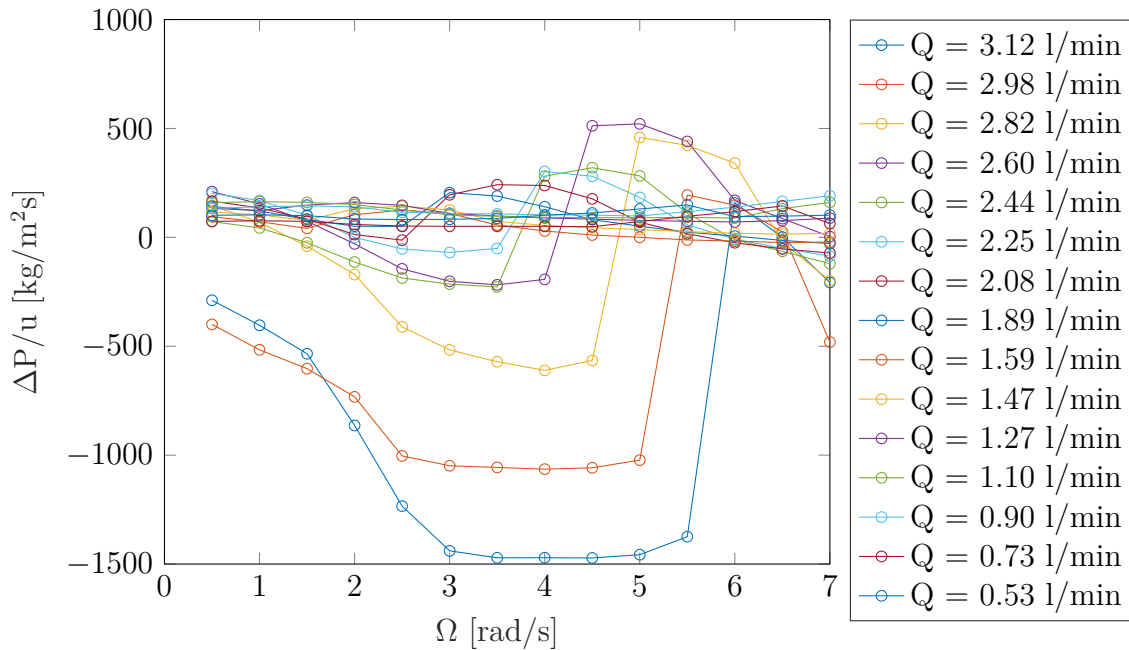

Figure 5.16: Normalized pressure $\Delta P_{5-6}/u$ as function of the rotation rate for different flow rates. In case of geostrophy, $\Delta P_{5-6}/u \sim \Omega$.
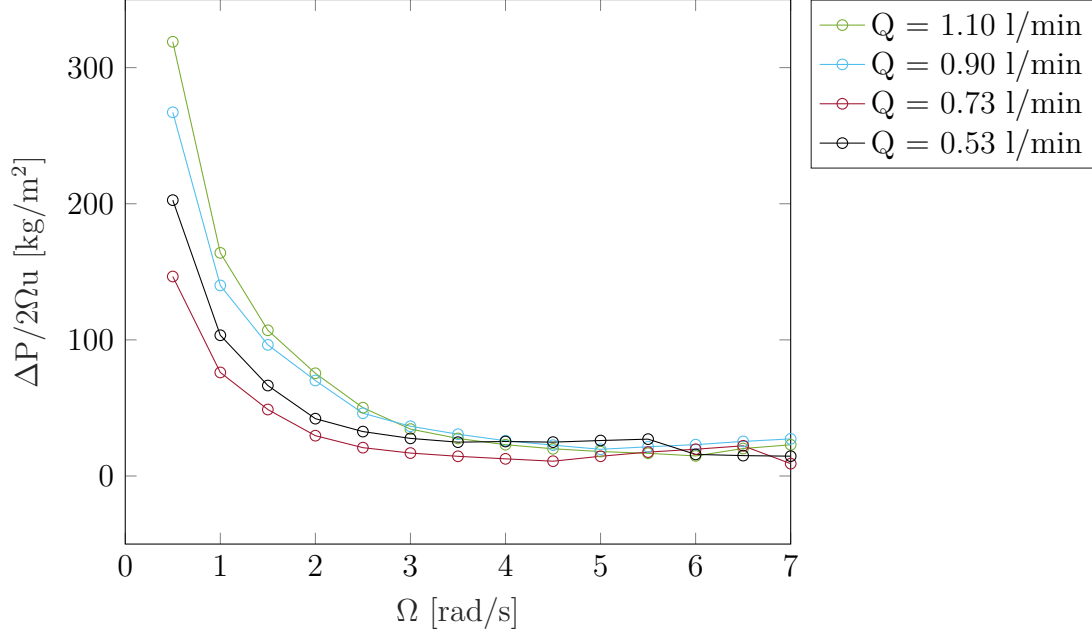
Figure 5.17: Normalized pressure $\Delta P_{5-6}/2\Omega u$ as function of the rotation rate for different flow rates. In case of geostrophy, $\Delta P_{5-6}/2\Omega u =$ constant.

The experiments show that geostrophy might only be present for the highest rotation rates. Therefore, we look in the simulations at the highest two rotation rates ($Omega = 5$ and $\Omega = 6$ rad/s) in search for geostrophy. From section 2.1, that in we know the geostrophic balance $2fu = -\partial P/\partial y$. Figure 5.18 shows $\partial P/\partial y + 2uE^{-1}$ in the yz-plane at $x = -0.65$ for the simulations. This is the plane where the orifices 5 and 6 are present. Geostrophy is present when $\partial P/\partial y + 2uE^{-1} \approx 0$.

The jet, visible in the center of Figure 5.18, is far from geostrophic. On the left and right of the jet geostrophy seems locally present in the y-direction. However, for $\Omega = 6$ rad/s less geostrophy seems present than for $\Omega = 5$ rad/s which is not what we expected. Therefore, $\partial P/\partial y + 2uE^{-1}$ is observed in the xy-plane shown in Figure 5.19 at $z = 0.45$. Here we see as observed in Figure 5.18 that near the inlet, geostrophy is more present for $\Omega = 5$ rad/s than for $\Omega = 6$ rad/s. Near the outlet of the container more geostrophy is present in the center than near the inlet. As expected, more geostrophy is present for $\Omega = 6$ rad/s than for $\Omega = 5$ rad/s. Geostrophy is not present near the walls on the top and bottom of the figure. It seems that the geostrophy might best be measured near the exit of the container instead of near the inlet. The current pressure difference is measured over orifice 5 and 6 that are located close to the walls. From the simulations seems that the pressure difference might best be measured more in the center. The experiments do not show geostrophy for $Q_{nr} = 1.59 \pm 0.07$ l/min. This is in agreement with the simulations since at the position of orifice 5 and 6 near the inlet no geostrophy is found. Based on the flow rate where geostrophy is found in the experiments, lower flow rates should be used in both simulations and experiments in order to compare them.
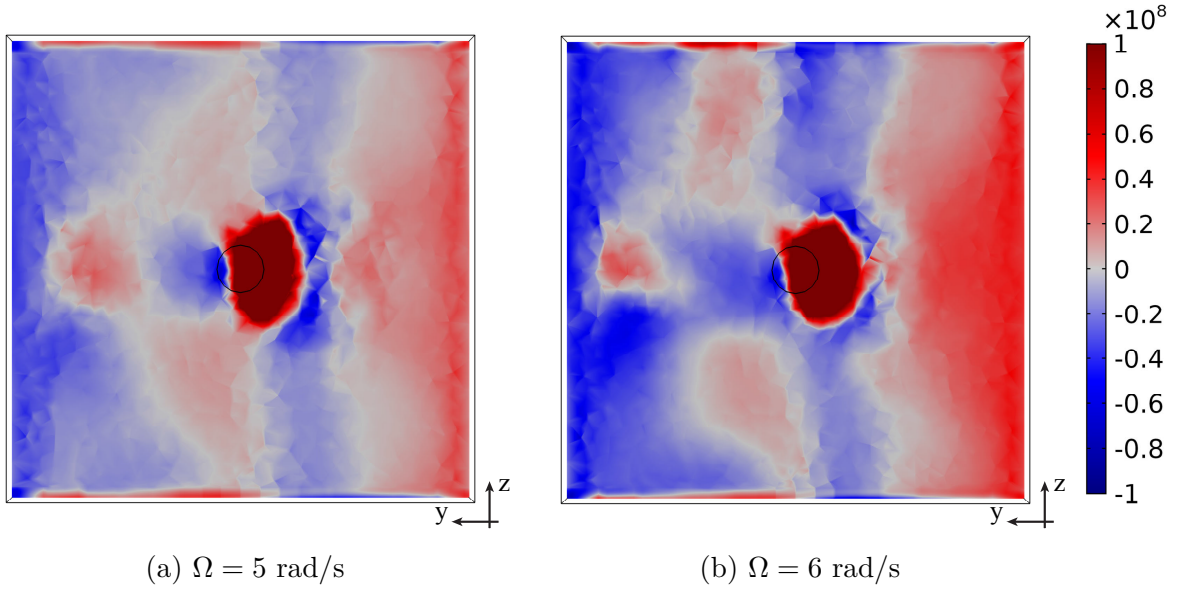
(a) $\Omega = 5$ rad/s   (b) $\Omega = 6$ rad/s

Figure 5.18: Value of $\partial P/\partial y + 2uE^{-1}$ in a slice of the yz-plane at $x = -0.65$ from the simulations. The pressure $P_0 = 1.85 \cdot 10^9$ is used, corresponding to $Q_{nr} = 1.59$ l/min. In (a) $\Omega = 5$ rad/s and in (b) $\Omega = 6$ rad/s.

(a) $\Omega = 5$ rad/s   (b) $\Omega = 6$ rad/s

Figure 5.19: Value of $\partial P/\partial y + 2uE^{-1}$ in a slice of the xy-plane at $z = 0.45$ of the container from the simulations. The pressure $P_0 = 1.85 \cdot 10^9$ is used, corresponding to $Q_{nr} = 1.59$ l/min. In (a) $\Omega = 5$ rad/s and in (b) $\Omega = 6$ rad/s. The inlet is on left of the container and the outlet on the right.
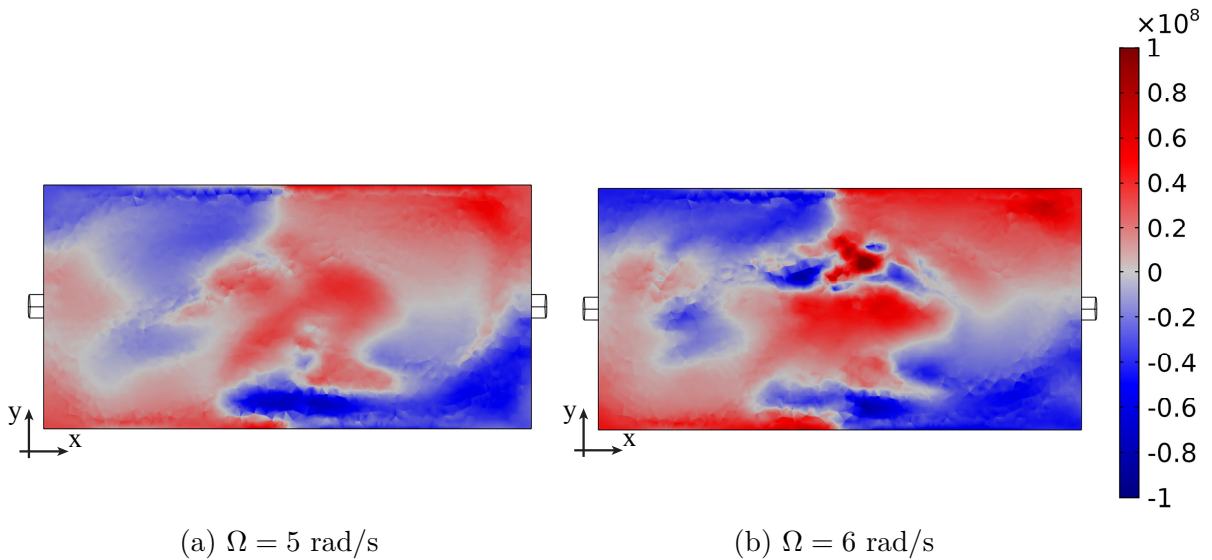
5.4.1 Spectra of the cross-channel pressure difference

In the rotating container, waves can be present as discussed in section 2.2. A frequency analysis is performed on the recorded signal of the pressure difference of 150 s. This is done to visualize what frequencies and waves are present in the flow. Figure 5.20 shows the frequency spectrum for $Q_{nr} = 0.53$ l/min and $\Omega = 6$ rad/s. On the left of $\omega/2\Omega = 0.5$, a peak is visible. This peak is within the inertial wave regime so it could represent inertial

waves in the container. Another possibility, in previous rotating laboratory experiments it was found that at $\omega/2\Omega = 0.5$ a peak can be present as an effect of the earth rotation [30]. As found in section 5.3, a vortex can be present below orifice 6 for high rotation rates. A vortex affects the angular momentum locally in a rotating system. An anticyclonic vortex results in a locally weaker sensed Ω and a cyclonic vortex results in a locally stronger sensed Ω. This means that an anticyclonic vortex induces a shift in frequency to a lower frequency and a cyclonic vortex to a higher frequency. Hence, the peak at $\omega/2\Omega = 0.5$ as an effect of the earth rotation, can be shifted to a slightly lower frequency due to the anticyclonic vortex underneath orifice 6. This might explain the frequency peak found in Figure 5.20.

On the right side in the spectrum, a decay with the power -1 is visible starting approximately at $\log_{10}(\omega/2\Omega) = 0.75$. This decay also known as pink noise, is artificial and is caused by the sampling rate used in the experiments [31]. Therefore, this part of the spectrum will not further discussed.
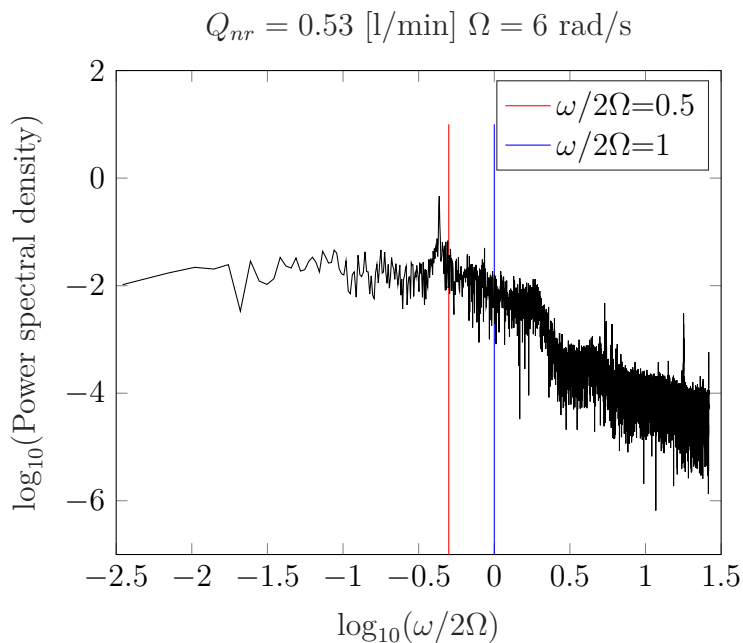

Figure 5.20: The log-log frequency spectrum of measured pressure difference ΔP_{5-6} for $Q_{nr} = 0.53$ l/min and a rotation rate $\Omega = 6$ rad/s.

Figure 5.21 shows the frequency spectrum for $Q_{nr} = 2.25$ l/min and $\Omega = 7$ rad/s. In this figure, no peaks are present in the inertial wave regime. However, Figure 5.21 shows a peak on the right of $\omega/2\Omega = 1$ around $\log_{10}(\omega/2\Omega) = 0.22$ which was also, albeit less dominant, present in Figure 5.20. In all spectra from the measured pressure difference ΔP_{5-6} in Figure 5.11, it is observed that this peak is present at a constant frequency of approximately 3.6 Hz. Hence, this frequency is not dependent on the flow or rotation rate. To check whether this peak is a result of the rotation on the flow, the spectrum of the nonrotating flow is observed and shown in Figure 5.22. The peak with a frequency of 3.6 Hz is still visible even without rotation. This suggest that this peak is a property of some component in the setup and not an effect of rotation. Due to the limitations of the pump, we checked whether the pump causes this peak. Therefore, the spectrum of the recorded flow rate signal for $Q_{nr} = 2.25$ l/min without rotation was analyzed and is

shown in Figure 5.23. If this constant peak in the pressure measurements is caused by an effect in the pump, the peak is also expected in the measured flow signal. Since this is not the case, the peak is not caused by the pump and has to be caused by some other component of the setup.
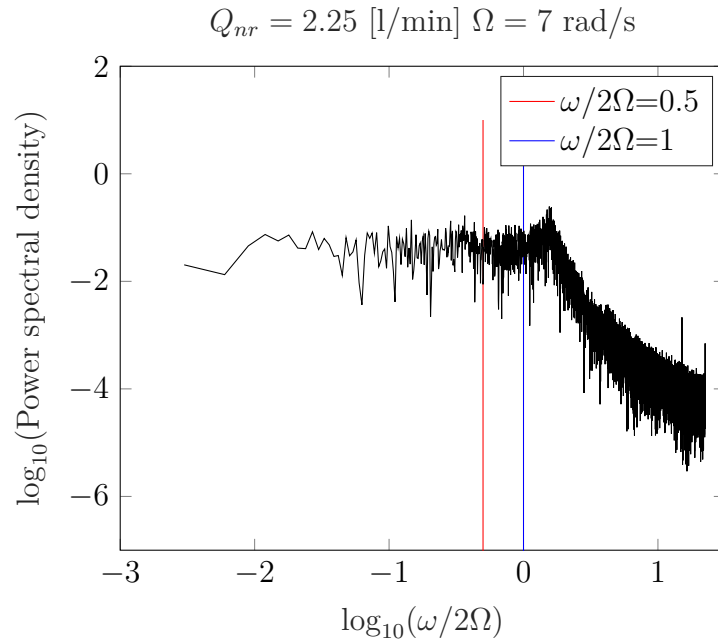

Figure 5.21: The log-log frequency spectrum of measured pressure difference ΔP_{5-6} for $Q_{nr} = 2.25$ l/min and a rotation rate $\Omega = 7$ rad/s.
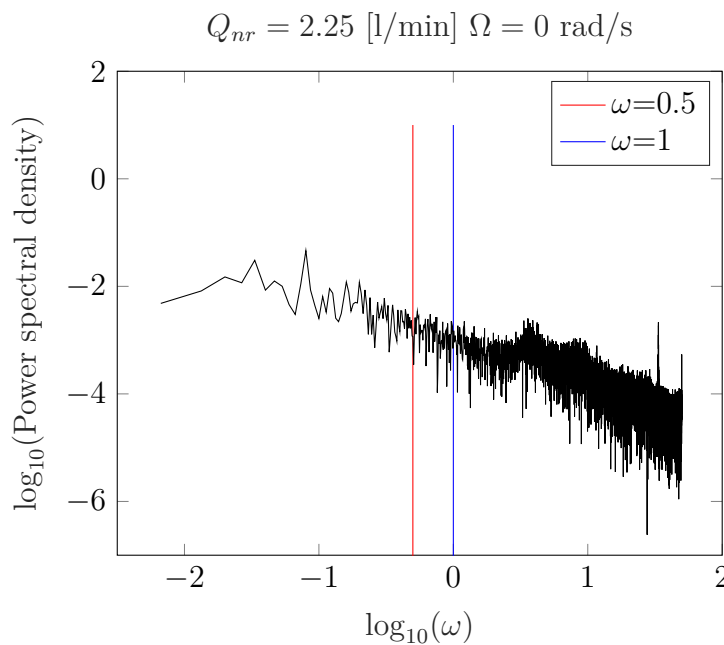

Figure 5.22: The log-log frequency spectrum of measured pressure difference ΔP_{5-6} for $Q_{nr} = 0.53$ l/min and no rotation.
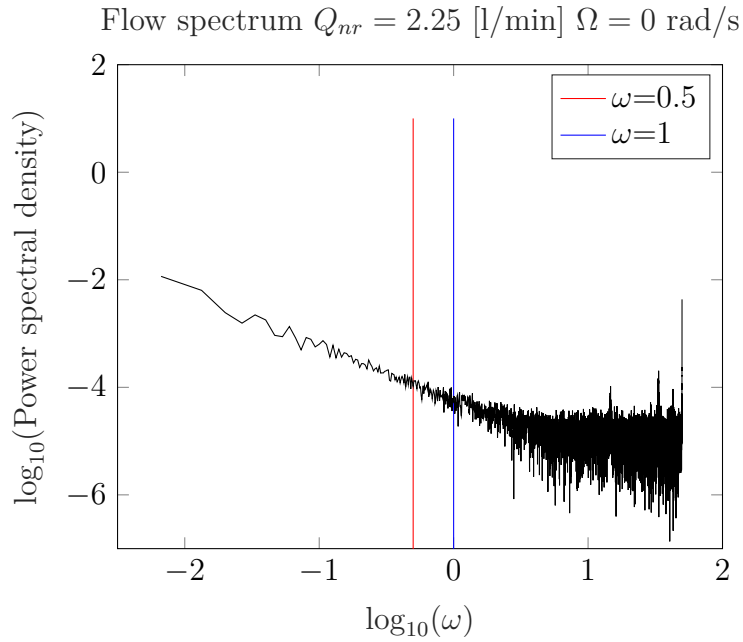
Figure 5.23: The log-log frequency spectrum of flow rate signal Q for $Q_{nr} = 2.25$ l/min and no rotation.

5.5 Tilted container

When the container is placed under an angle, additional Rossby waves are expected in the container. The tilted container discussed in this section is tilted under an angle of $20°$.

5.5.1 Flow rate

To observe the effect of the tilt on the flow, $Q_{nr} = 1.59 \pm 0.07$ l/min is used for rotation rates of 0 to 6 rad/s. The relative change in the flow rate ΔQ_{rel} as function of the rotation rate is shown in Figure 5.24 for the container under a tilt of $20°$ and without tilt. The error bars represent the standard deviation in the flow signal.
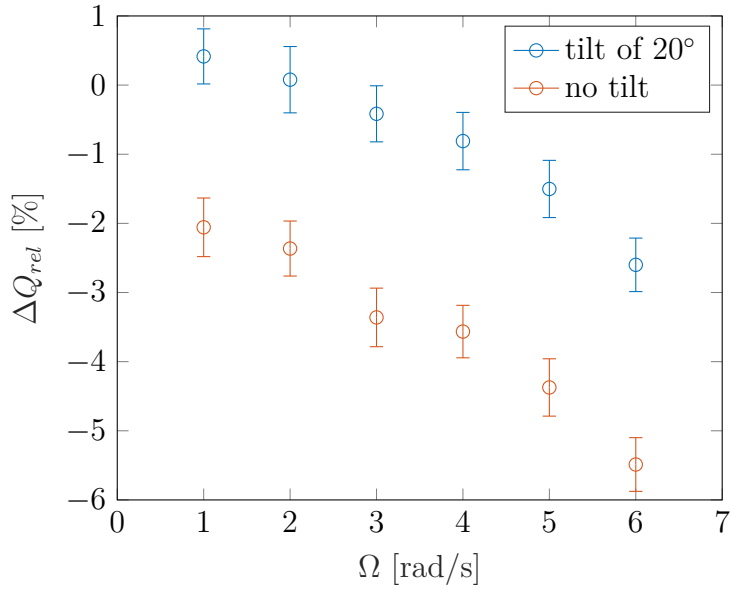
Figure 5.24: Relative change in flow rate ΔQ_{rel} as function of the rotation rate for $Q_{nr} = 1.59$ l/min with a tilt of 20° and without a tilt. The error bars represent the standard deviations in the averaged flow signal.

Figure 5.24 shows that the flow rate increases for the rotation rates of 1 and 2 rad/s. However, within the error bar this change in flow rate might as well be 0 for 1 rad/s and even negative for 2 rad/s. Compared to the non-tilted case, it is seen that the flow is enhanced with a tilt and decreased without a tilt. To ensure the pump is not causing the increase at 1 and 2 rad/s, the experiments should be repeated in the future with a more reliable pump. The flow rate decreases for the tilted container for rotation rates of 3 to 6 rad/s. Compared to the container without a tilt, the decrease is less strong. To what extend a certain angle affects the flow could be investigated in the future by repeating this experiment for several angles and comparing the changes in the flow rate.

5.5.2 Pressure

Unfortunately, it was not possible to measure the pressure difference between the orifices 5 and 6 in the tilted container for rotation rates larger than $\Omega = 1$ rad/s. This is because the pressure difference exceeds the maximum range of the pressure meter. The frequency is analyzed for $\Omega = 1$ rad/s for $Q_{nr} = 0.73$ and $Q_{nr} = 1.59$ l/min. The frequency spectra of both flow rates are indicated in black in the Figures 5.25(a) and 5.26(a), respectively. These measurements are repeated 10 times to reduce noise and averaged in the Fourier spectrum (shown in the pink line in the Figures 5.25(a) and 5.26(a)). These spectra are compared to the spectra for the same flow and rotation rates for a container without a tilt. In the Figures 5.25(b) and 5.26(b) the spectra of the flow rates of 0.73 and 1.59 l/min are shown without a tilt, respectively. From this comparison is found that there are no other peaks visible in the tilted spectrum compared to the spectrum without a tilt. The Rossby waves might not be predominantly present since the rotation rate is quite low.
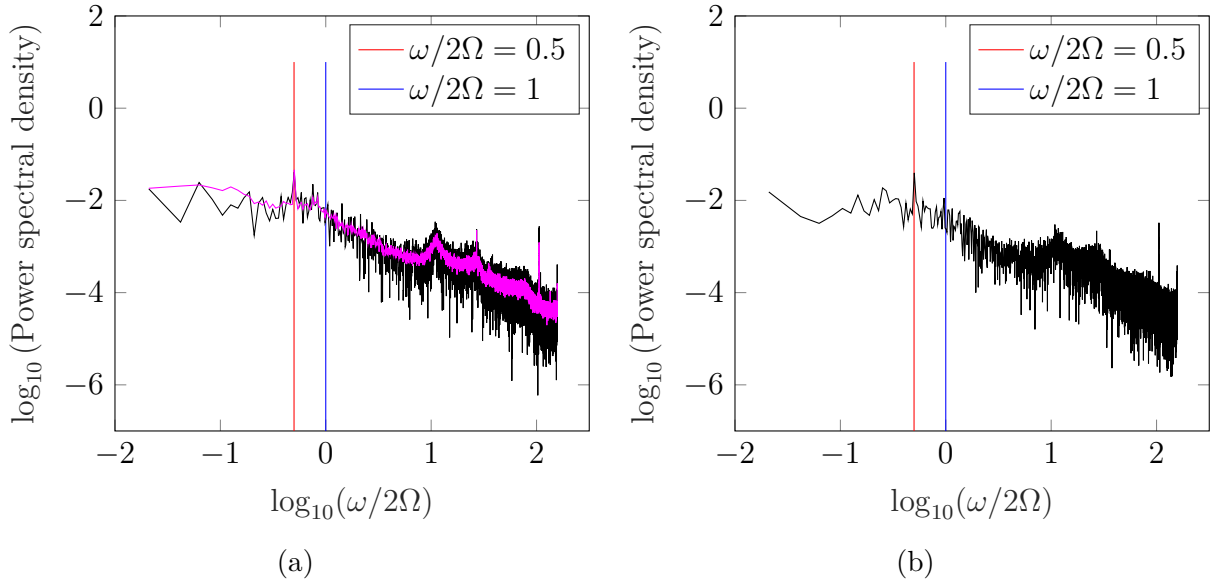
Figure 5.25: The log-log frequency spectrum of measured pressure difference ΔP_{5-6} for $Q_{nr} = 0.73$ l/min and a rotation rate $\Omega = 1$ rad/s. (a) The container is tilted under 20°, the black line represents one spectrum analysis, the pink line represents an average over ten spectra to reduce noise. (b) The spectrum for a container without a tilt is shown.

Figure 5.26: The log-log frequency spectrum of measured pressure difference ΔP_{5-6} for $Q_{nr} = 1.59$ l/min and a rotation rate $\Omega = 1$ rad/s. (a) The container is tilted under 20°, the black line represents one spectrum analysis, the pink line represents an average over ten spectra to reduce noise. (b) The spectrum for a container without a tilt is shown.
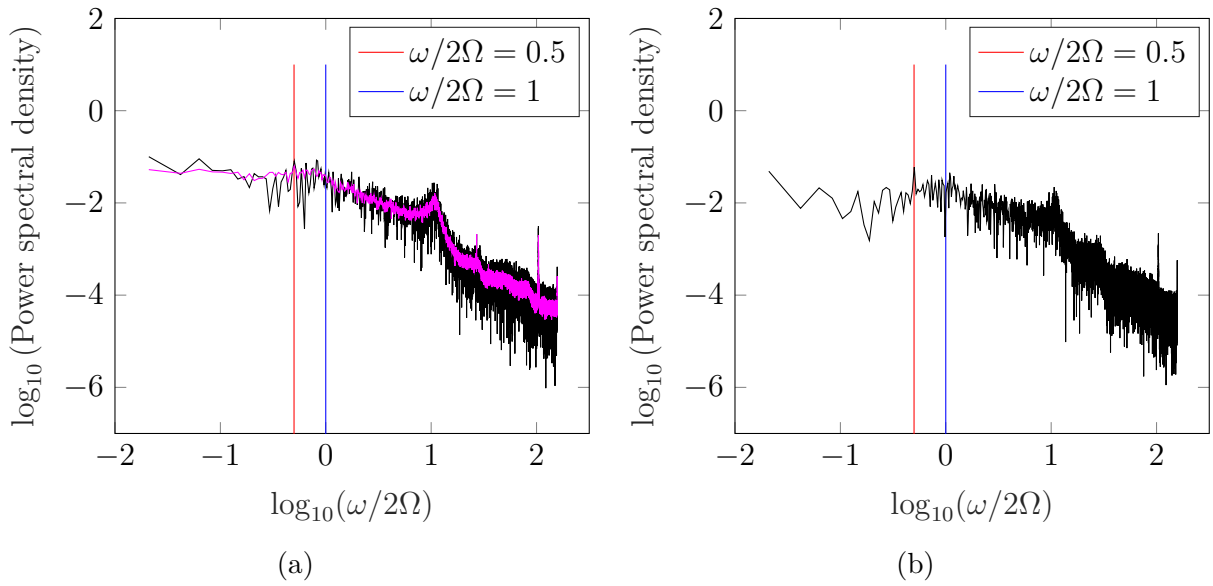
Chapter 6

Conclusion

The goal of this project is to understand how rotation affects the flow in a cavity and determine whether the flow is accelerated or retarded. This is studied by using simulations and experiments. In the experiments, a flow is generated in the container by a pump and measured using a flow meter. The setup is placed on top of a rotating table to investigate how the flow rate changes due to the rotation rate. On top of the container, a pressure meter measures the cross-channel pressure difference, which is used to search for geostrophy and the presence of waves. In the simulations the experimental setup is reproduced.

The results from the simulations and experiments indicate that the flow rate is less sensitive to rotation than previously thought. The experiments on the flow rate show a maximum retardation of 10% of the nonrotating flow rate. This is in contrast with previous results where differences reached up to 30% [3], and confirms the suspicion that those experiments were strongly affected by a misalignment of the table. In spite of the improvements in the experimental setup, the accuracy of the pump is not high enough to generate a flow rate without large fluctuations. Hence, the changes in the flow rate are highly susceptible to the pump. The flow pattern obtained from the visualization of the laboratory experiments and simulations show secondary flows and vortices. Since the position over which the cross-channel pressure difference is measured is close to one of these vortices, this might affect this measurement. Geostrophy is only found for the lowest flow rates and highest rotation rates. This indicates that the majority of the studied flow rates are too large for a geostrophic flow. The range of the pressure meter was insufficient to obtain a useful measurement for the tilted container.

This study indicates that the flow in the container is more delicate than previously thought. The fluctuations in the pump throughput are too large to accurately quantify the effect of rotation on the flow. Nonetheless, some trends are visible. We see that rotation inhibits the throughflow for a container without a tilt. A tilted container inhibits the throughflow less and might even increase the throughflow but due to the pump's inaccuracy no hard statement can be made. We do see presence of inertial waves in the Fourier spectrum, but are unable to identify Rossby waves for the tilted container. In this way, it is clear that multiple complex flow phenomena arise in the flow through a cavity when subjected to background rotation. The interaction and net effect of these phenomena is still a matter for future research.

Chapter 7

Outlook

First and most important of all, great care should be taken in selecting an accurate pump. The results show a large variability in the flow rate from the pump which is larger than the measured differences in the flow rate due to rotation. To perform reliable experiments, the fluctuations in the flow rate from the pump should be smaller than the changes induced by the rotation. The geostrophy measurements show that geostrophy is only found for the lowest flow rates in the current flow range. This indicates that we should measure in a lower flow range to have a geostrophic flow.

The visualization we applied was only qualitative, since Particle Image Velocimetry (PIV) is too challenging for the flow velocities. When lower flow velocities are attained in future experiments, PIV could give quantitative information about the flow and give better insight into the flow pattern. When PIV is performed on the tilted container, wave attractors and Rossby waves might be visible as well.

The visualization shows the presence of a vortex underneath orifice 6, which is used to measure the cross-channel pressure difference. In addition, the simulations show a higher chance of geostrophy near the outlet of the container. Both these findings indicate that measuring the cross-channel pressure difference near the exit of the container gives more insight into the flow.

It was expected that in the tilted container Rossby waves would be present in the frequency spectrum. Due to the range of the pressure meter, the measurements could only be performed for a rotation rate of 1 rad/s. To investigate the presence of Rossby waves in the frequency spectrum, a pressure meter with a larger range should be used.

7.1 Practical remarks

In the process of building and testing the setup some practical aspects came along that should be taken into account. A good thought should be given to the entrance height of the container. When the container is tilted, the entrance height should be kept constant to ensure a constant flow rate for a set applied voltage on the pump.

A mirror is placed underneath the container to visualize the flow, the entrance height of the container should be at a non-tilted height which allows enough space for the mirror underneath the container when tilted.

Chapter 8

Bibliography

[1] G.J.van Heijst. Geophysical fluid dynamics lecture notes. 2017.

[2] J. Pedlosky. *Geophysical fluid dynamics*. 1987.

[3] L. Maas. Experiments on rotating flows: impact of rotation on flow through tilted rectangular ducts. 2008. URL `https://www.staff.science.uu.nl/~maas0131/files/maasFluxesStructures2007p.pdf`.

[4] J. Pallares, F. Grau, and L. Davidson. Pressure drop and heat transfer rates in forced convection rotating square duct flows at high rotation rates. *Physics of Fluids*, 17 (7), 2005.

[5] Ugur Kesgin. Study on the design of inlet and exhaust system of a stationary internal combustion engine. *Energy Conversion and Management*, 46(13), 2005.

[6] NASA and J. Descloitres. Depression in the Pacific ocean, 2012. URL `https://visibleearth.nasa.gov/view.php?id=63513`.

[7] G. Mårtensson, J. Gunnarsson, A. Johansson, and H. Moberg. Experimental investigation of a rapidly rotating turbulent duct flow. *Experiments in Fluids*, 33(3), 2002.

[8] J. Hart. Instability and secondary motion in a rotating channel flow. *Journal of Fluid Mechanics*, 45(2), 1971.

[9] K. Nandakumar, H. Raszillier, and F. Durst. Flow through rotating rectangular ducts. *Physics of Fluids A*, 3(5), 1991.

[10] O. Phillips. Energy transfer in rotating fluids by reflection of inertial waves. *Physics of Fluids*, 6(4), 1963.

[11] L. Maas and F. Lam. *Geometric focusing of internal waves*, volume 300. 1995.

[12] L. Maas. Wave focusing and ensuing mean flow due to symmetry breaking in rotating fluids. *Journal of Fluid Mechanics*, 437, 2001.

[13] C. Rodda. The ocean in a tank: numerical simulations on the wave-mean flow interactions in a rotating box. Technical report, University of Trieste, 2015.

[14] M. Duran-Matute and L. Maas. Private communication, 2019.

[15] P. Kundu and I. Cohen. *Fluid mechanics*. 2008.

[16] P. Childs. *Rotating Flow*. 2011.

[17] H. Greenspan. *The theory of rotating fluids*. 1968.

[18] L Messio, C Morize, M Rabaud, and F Moisy. Experimental observation using particle image velocimetry of inertial waves in a rotating fluid. *Experiments in Fluids*, 44(4), 2008.

[19] L. Maas. On the amphidromic structure of inertial waves in a rectangular parallelepiped. *Fluid Dynamics Research*, 33(4), 2003.

[20] J. Hazewinkel. *Attractors in stratified fluids*. Utrecht University, 2010.

[21] L. Maas. Wave attractors: linear yet nonlinear. *International Journal of Bifurcation and Chaos*, 15(9), 2005.

[22] Wave attractors and the asymptotic dissipation rate of tidal disturbances. *Journal of Fluid Mechanics*, 543, 2005.

[23] L. Jouve and G. Ogilvie. Direct numerical simulations of an inertial wave attractor in linear and nonlinear regimes. *Journal of Fluid Mechanics*, 745, 2014.

[24] C. Cavallini. *Quasi-geostrophic theory of oceans and atmosphere*. Springer, 2013.

[25] Van Heijst, G.J. Topography effects on vortices in a rotating fluid. *Meccanica*, page 451, 1994.

[26] B. Cushman-Roisin and J. Beckers. Introduction to Geophysical Fluid Dynamics Physical and Numerical Aspects. *International Geophysics*, 101, 2011.

[27] van de Vooren, A. The Stewartson layer of a rotating disk of finite radius. *Journal of Engineering Mathematics*, 26(1), 1992.

[28] G.J.van Heijst. Syllabus Roterende stromingen. 1979.

[29] COMSOL. COMSOL Multiphysics 5.3a reference guide. 2017.

[30] P. Meunier, C. Eloy, R. Lagrange, and F. Nadal. A rotating fluid cylinder subject to weak precession. *Journal of Fluid Mechanics*, 599, 2008.

[31] L. Ward and P. Greenwood. 1/f noise. *Scholarpedia*, 2(12), 2007.

Appendix A

Flow structure

The following Matlab scripts are used to create a flow pattern from the visualization. We are only interested in the particles that move, so it is necessary to remove all bright, stationary spots from the images by applying a background correction. This background is calculated (Background filter) by summing 200 frames and dividing this by 100, i.e. by averaging the image over 100 frames. Then this background is subtracted from all frames (Background correction) that we have analyzed. Next, 100 frames are added to create a flow pattern (Creating flow pattern). These 100 frames correspond to approximately 3.0 s.

Background filter

```matlab
function background = backgroundfilter(ROI, filenames, ndata)
%% with this function the 'background'-filter for the ROI can be calculated
% ROI:  is an array in the shape [x1,y1,x2,y2] which define the rectangular
% ROI
% filenames: insert the filename for the files, so this script knows which
% file it needs to load
% ndata: total number of files that are needed to calculate the
% backgroundfilter

temp = imread([filenames,num2str(1),'.tif']);
bg_temp = temp(ROI(1):ROI(3),ROI(2):ROI(4))*0;
for i=1:ndata
    fig = imread([filenames,num2str(i),'.tif']);
    bg_temp =bg_temp+ fig(ROI(1):ROI(3),ROI(2):ROI(4));
end
background = bg_temp/ndata;
end
```

Background correction

```matlab
function frames = backgroundcorrected(ROI, filenames, ndata)

% this function corrects all the frames for the present background.
ROIX = ROI(3)-ROI(1)+1;
ROIY = ROI(4)-ROI(2)+1;


background = backgroundfilter(ROI, filenames, ndata);
frames = zeros(ROIX,ROIY,ndata);
for i=1:ndata
```

```matlab
        fig = imread([filenames,num2str(i),'.tif']);
        frames(:,:,i) = fig(ROI(1):ROI(3),ROI(2):ROI(4))-background;
    end

end
```

Creating flow pattern

```matlab
%% declare all simple variables:
% ROI = the region of interest, in the form of X_1, Y_1, X_2, Y_2 where
% X,Y_1 is the lower left corner of the ROI and X_2, Y_2 the upper right
% corner.
% ROIX          = total array elements in the X direction
% ROIY          = total array elements in the Y direction
% filenames     = the 'general' name of the files. Looping will be done
% elsewhere.
% ndata         = the total number of frames to be included. Currently this
% is also the number of frames that is used in the background correction.
% threshold     = the value below which the values are cut- off to zero.
%n              = the total number of frames shown in the plot.
ROI = [301,191,886,1415];
ROIX = ROI(3)-ROI(1)+1;
ROIY = ROI(4)-ROI(2)+1;
filenames = '05_4V2_0rads_center_';
ndata = 200;
threshold = 2000;
nb = 1;
ne = 100;
%% declare arrays:
% frames2       = array that contains data for all the frames as seperate
% entries.
% frames3       = array that contains a summation of n frames.
frames2 = zeros(ROIX,ROIY,ndata);
frames3 = zeros(ROIX,ROIY);

frames = backgroundcorrected(ROI,filenames,ndata);

frames2 = zeros(ROIX,ROIY,ndata);
for l=1:ndata
    for i=1:ROIX
      for j=1:ROIY
            if frames(i,j,l) >= threshold
                frames2(i,j,l) = 1;
            end
      end
    end
end

frames3 = zeros(ROIX,ROIY);
for i=nb:ne
    frames3 = frames3 + frames2(:,:,i);
    imshow(frames3)
    pause(0.2)
end

imshow(frames3)
```